

# $Tl_2Ba_2CuO_{6+\delta}$ Brings Spectroscopic Probes Deep Into the Overdoped Regime of the High- $T_c$ Cuprates

DC Peets, JDF Mottershead, B Wu, IS Elfimov, R Liang, WN  
Hardy, DA Bonn, M Raudsepp<sup>†</sup>, NJC Ingle and A Damascelli

Department of Physics and Astronomy, University of British Columbia,  
Vancouver, BC V6T 1Z1 Canada

<sup>†</sup> Department of Earth and Ocean Sciences, University of British Columbia,  
Vancouver, BC V6T 1Z4 Canada

E-mail: bonn@physics.ubc.ca and damascelli@physics.ubc.ca

**Abstract.** Single-particle spectroscopic probes, such as scanning tunneling and angle-resolved photoemission spectroscopy (ARPES), have provided us with crucial insights into the complex electronic structure of the high- $T_c$  cuprates, in particular for the under and optimally doped regimes where high-quality crystals suitable for surface-sensitive experiments are available. Conversely, the elementary excitations on the heavily overdoped side of the phase diagram remain largely unexplored. Important breakthroughs could come from the study of  $Tl_2Ba_2CuO_{6+\delta}$  (Tl2201), a structurally simple system whose doping level can be tuned from optimal to extreme overdoping by varying the oxygen content. Using a self-flux method and encapsulation, we have grown single crystals of Tl2201, which were then carefully annealed under controlled oxygen partial pressures. Their high quality and homogeneity are demonstrated by narrow rocking curves and superconducting transition widths. For higher dopings, the crystals are orthorhombic, a lattice distortion stabilized by O interstitials in the TlO layer. These crystals have enabled the first successful ARPES study of both normal and superconducting-state electronic structure in Tl2201, allowing a direct comparison with the Fermi surface from magnetoresistance and the gap from thermal conductivity experiments. This establishes Tl2201 as the first high- $T_c$  cuprate for which a surface-sensitive single-particle spectroscopy and a comparable bulk transport technique have arrived at quantitative agreement on a major feature such as the normal state Fermi surface. The momentum dependence of the ARPES lineshape reveals, however, an unexpected phenomenology: in contrast to the case of under- and optimally-doped cuprates, quasiparticles are sharp near  $(\pi, 0)$ , the antinodal region where the gap is maximum, and broad at  $(\pi/2, \pi/2)$ , the nodal region where the gap vanishes. This reversed quasiparticle anisotropy past optimal doping, and its relevance to scattering, many-body, and quantum-critical phenomena in the high- $T_c$  cuprates, are discussed.

Submitted to New Journal of Physics (September 4, 2006).

## 1. Introduction

The cuprate superconductors can be tuned through a remarkable progression of states of matter by doping charge carriers into the  $\text{CuO}_2$  planes [1]. The most generic feature of this tuning is a sequence from an antiferromagnetic insulator, through a doping range where the superconducting critical temperature builds to a maximum (optimal doping) and then dies away again at higher doping, in the so-called overdoped regime (Fig. 1). This sequence contains three separate touchstones for an understanding of the cuprates: the Mott insulator, which is known to result from very strong electron-electron repulsion and is antiferromagnetically ordered, the  $d$ -wave superconductor, and the overdoped metal. The latter is widely believed to exhibit less exotic normal-state properties and might be understood through Fermi liquid theory. Over the last two decades, a great deal of experimental work has been done on undoped, underdoped, and optimally doped cuprates, aiming at elucidating the connection between the antiferromagnetic insulator and high- $T_c$  superconductor (HTSC), and the role of electronic correlations in the emergence of superconductivity. However, the testing of Fermi liquid theory in the overdoped regime has been severely hampered by a lack of compounds that can actually be doped to this high level and are suitable for a wide range of experimental techniques.

In the struggle to understand high- $T_c$  superconductivity, the quest for better materials to study remains key. Researchers want samples that can be grown very cleanly, can be doped over a very wide range of the phase diagram, and are suitable for a variety of bulk and surface measurements. Surface-sensitive techniques in particular, such as angle-resolved photoemission spectroscopy (ARPES) [2, 3] and scanning tunneling microscopy (STM) and spectroscopy (STS) [4], introduce additional constraints with regard to sample requirements. These highly sophisticated spectroscopic probes can be used to obtain information on the single-particle excitation spectrum of a solid — i.e. the spectral function  $A(\mathbf{k}, \omega)$  that can be calculated in terms of the electron Green's function starting from the microscopic many-body Hamiltonian of the system [5] — but only if the material can be cleaved to expose a well-defined and stable surface (i.e. which does not reconstruct, obscuring the bulk electronic structure).

A summary of the approximate doping range explored by ARPES on different HTSC families is given in Fig. 1. On the undoped side of the phase diagram ( $p=0$ ), the parent compounds  $\text{Ca}_2\text{CuO}_2\text{Cl}_2$  and  $\text{Sr}_2\text{CuO}_2\text{Cl}_2$  yield excellent cleaved [001] faces that have allowed ARPES studies of the electronic structure of the correlated antiferromagnetic insulator and of the magneto-elastic interactions associated with the propagation of a single hole in the two-dimensional spin background [6, 7, 8]. Via hole doping, one can drive these materials through a metal-insulator transition and enter the superconducting dome (in this paper we will focus on the hole-doped side of the phase diagram). For instance, recent STM, STS [9], and ARPES [10] experiments on the underdoped superconductor  $\text{Ca}_{2-x}\text{Na}_x\text{CuO}_2\text{Cl}_2$  have suggested the existence of new electronic ordering phenomena in the doping region between the insulator and the superconductor, possibly in the form of glassy electronic behavior or a surface-nucleated phase transition

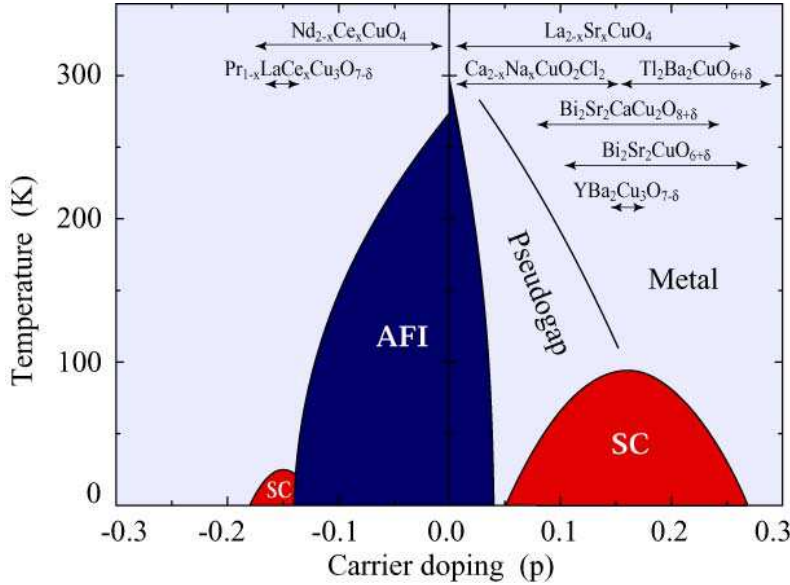


**Figure 1.** Generic temperature-doping phase diagram for both electron ( $p < 0$ ) and hole-doped ( $p > 0$ ) cuprates. The doping range actually explored by ARPES for those material families more extensively studied is indicated by the corresponding arrows.

as more conventional long-range charge order was not observed in scattering studies [11]. Near optimal doping, where the cuprates exhibit their highest superconducting critical temperatures,  $\text{YBa}_2\text{Cu}_3\text{O}_{7-\delta}$  stands out as the cleanest material and has been used extensively in bulk-sensitive studies of the normal and superconducting properties, such as the symmetry of the order parameter [12, 13, 14], superfluid density [15], charge and thermal transport [16], low-energy electrodynamics [17, 18], vibrational and magnetic excitation spectra [19, 20]. Unfortunately, this material is complicated by the presence of CuO-chain layers and does not have a neutral [001] cleavage plane for surface-sensitive techniques. In particular,  $\text{YBa}_2\text{Cu}_3\text{O}_{7-\delta}$  cleaves between the chain layer and the BaO layer. BaO surfaces have had the nearest source of dopants (the CuO chains) removed, so that their hole-doping is uncertain. STS shows that the CuO chain surfaces are characterized by prominent surface density waves [21] and differ substantially from the bulk. They exhibit surface states, as seen in ARPES [22], and possess unavoidable doping disorder. These problems have severely limited the availability of single-particle spectroscopy data from ARPES [23, 24], STM, and STS [21, 25].

Extensive ARPES investigations have been performed on  $\text{La}_{2-x}\text{Sr}_x\text{CuO}_4$  [26], over a broad doping range extending from the undoped insulator ( $x = 0$ ) to the overdoped superconductor ( $x = 0.22$ ; note that  $x = p$  for this compound). This system, however, is affected by severe cation disorder associated with La-Sr substitution right next to the  $\text{CuO}_2$  plane, as well as lattice, charge, and magnetic instabilities, which might provide an explanation for why the maximum  $T_c$  in this compound is suppressed with respect to other single-layer materials [27]. In turn, many of the key bulk-sensitive measurements requiring perfect crystals and long mean free paths could not be performed for this

material family. In addition, neither STM nor STS experiments have been successful so far on cleaved  $\text{La}_{2-x}\text{Sr}_x\text{CuO}_4$ , probably because both the  $\text{CuO}_2$  and  $\text{La}_{1-\frac{x}{2}}\text{Sr}_{\frac{x}{2}}\text{O}$  surfaces are polar, with a charge  $z_{\text{CuO}_2} = -(2-x)$  and  $z_{(\text{La},\text{Sr})\text{O}} = (1-x/2)$ , and thus critically unstable. To date, the most rich and comprehensive spectroscopic information on high- $T_c$  cuprates from both STS and ARPES have been obtained on the Bi compounds, and in particular  $\text{Bi}_2\text{Sr}_2\text{CuO}_{6+\delta}$  and  $\text{Bi}_2\text{Sr}_2\text{CaCu}_2\text{O}_{8+\delta}$  [2, 3, 4]. However, similar to  $\text{La}_{2-x}\text{Sr}_x\text{CuO}_4$ , this family has greater problems with disorder than  $\text{YBa}_2\text{Cu}_3\text{O}_{7-\delta}$  [27], leaving a disconnection between materials for which we have the most information. This dilemma interferes with strict tests of the theory of high- $T_c$  superconductivity, in which one must connect the single particle excitations to the other physical properties and dynamic susceptibilities of the cuprates [28].

A further problem in the study of HTSCs is that, due to the high  $T_c$  values, the physical properties of the underlying normal state can be probed only at relatively high temperatures. This often makes the detailed interpretation of the experimental results more complex and less informative (e.g., charge and thermal conductivity, Hall number, magnetoresistance, etc.), or can even make some experiments completely unfeasible (as in the case of the de Haas-van Alphen effect). Alternatively, at least for certain techniques, one can access the low-temperature normal-state properties by suppressing superconductivity via the application of an external magnetic field. Once again however, due to the very high  $T_c$  and in turn the extraordinarily large value of the second critical field  $H_{c2}$ , this approach is precluded near optimal doping on the cleanest cuprates. Extreme overdoping is a means of reducing both  $T_c$  and  $H_{c2}$ , so that one can study both the superconducting and underlying normal states, but here most samples tend to be less clean because of the need to dope with large concentrations of cation impurities, such as Sr in  $\text{La}_2\text{CuO}_4$  and Pb in  $\text{Bi}_2\text{Sr}_2\text{CuO}_{6+\delta}$  [27]. In this case it can be unclear whether changes observed in the material's properties are attributable to the increased doping, or the increased scattering and/or other extrinsic effects. Due to these material and experimental limitations, the underlying normal state of HTSCs, the heavily overdoped side of the HTSC phase diagram, and the metallic state that emerges beyond the end of the superconducting dome have remained so far largely unexplored (Fig.1).

The most promising compound for investigating the deeply overdoped regime is the single-layer system  $\text{Tl}_2\text{Ba}_2\text{CuO}_{6+\delta}$  (Tl2201, see Fig. 2), whose natural doping range varies from optimal to extreme overdoping as one increases the oxygen content  $\delta$ . Tl2201 has two extremely flat  $\text{CuO}_2$  planes located far apart from each other in the body-centered unit cell; there are no complicating chain layers (as opposed to the Y-based cuprates), or bilayer band-splitting effects (as opposed to  $\text{Bi}_2\text{Sr}_2\text{CaCu}_2\text{O}_{8+\delta}$  and  $\text{YBa}_2\text{Cu}_3\text{O}_{7-\delta}$ ). Like La and Bi-based systems, Tl2201 can exhibit a cation non-stoichiometry but this consists in excess Cu substituting Tl in the  $\text{Tl}_2\text{O}_2$  double layer, farther removed from the  $\text{CuO}_2$  planes than the Bi-Sr or La-Sr substitutions that have been shown to have a large impact on the superconductivity of the Bi and La cuprates [27]. Tl2201 may be reversibly doped through interstitial oxygen and, near optimal doping, vacancies in the  $\text{Tl}_2\text{O}_2$  bilayer [29]. The ability to over dope a crystal reversibly

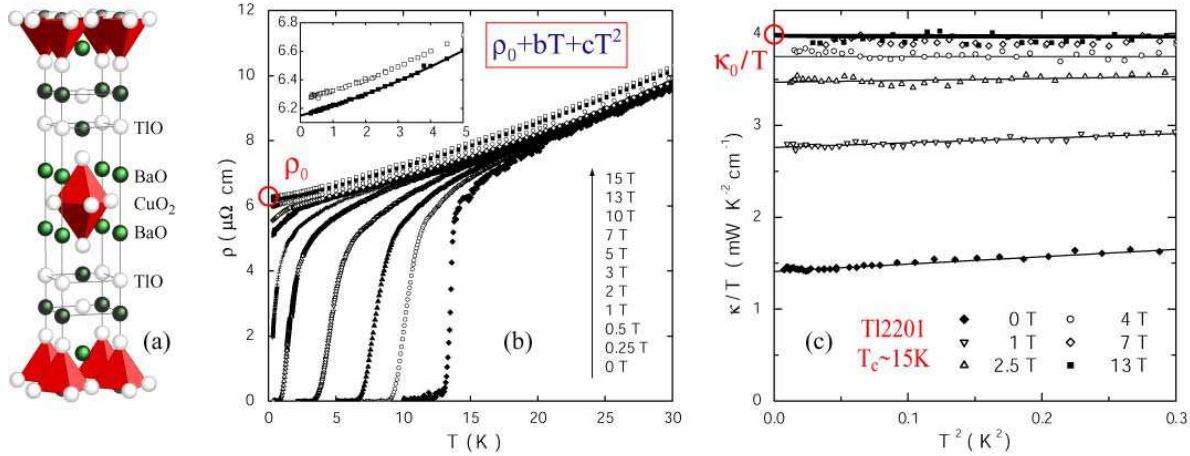


**Figure 2.** (a) Unit cell of Tl2201. (b,c) Electrical resistivity and thermal conductivity of overdoped Tl2201 ( $T_c \simeq 15$  K), plotted vs. temperature for different values of an external magnetic field applied normal to the CuO<sub>2</sub> planes (after Ref. [34]). From the  $T=0$  K intercepts of  $\rho(T)$  and  $\kappa(T)/T$ , the ratio  $\rho_0\kappa_0/T=0.99\pm0.01L_0$  was calculated ( $L_0=2.44\times10^{-8}$   $W\Omega K^2$  is Sommerfeld's value for the Lorenz ratio  $L\equiv\kappa/\sigma T$ ), which indicates that the Wiedemann-Franz law is obeyed in overdoped cuprates although the normal-state  $\rho(T)$  is dominated by a non Fermi-liquid like  $T$ -linear term (see inset).

from optimal doping to the full suppression of superconductivity, by changing its oxygen content alone, is a fortuitous property of Tl2201, although this has been successfully demonstrated over the whole doping range only on ceramic samples.

A variety of bulk properties have already been studied in Tl2201. At optimal doping, the pure  $d_{x^2-y^2}$  symmetry of the superconducting gap was confirmed by phase-sensitive measurements [30], and the so-called magnetic resonant mode at 47.5 meV was detected below  $T_c$  in neutron scattering experiments [31], the first time for a single-layer cuprate. The high sample quality has been recently demonstrated by measurements of angular magnetoresistance oscillations (AMRO), a bulk transport technique that requires the long mean free paths afforded by high purity and crystallinity [32]. The AMRO study of Tl2201 resulted in the first estimate of the normal state Fermi surface of a cuprate superconductor from a bulk sensitive probe. The combination of charge [33, 34] and heat [34] transport measured at low temperature on very overdoped Tl2201 in the normal state, by applying up to 13T magnetic fields to suppress superconductivity (see Fig. 2), allowed the Lorenz ratio  $L\equiv\kappa/\sigma T$  to be extracted. The value obtained,  $0.99\pm0.01L_0$ , allowed one to conclude that the Wiedemann-Franz law is obeyed in overdoped cuprates: the electronic carriers of heat are fermionic excitations of charge  $-e$ , suggesting that the low-energy excitations in overdoped cuprates might indeed be described in terms of Fermi-liquid quasiparticles [34]. At variance with the hints of Fermi-liquid-like behavior, however, the *ab*-plane resistivity is not purely described by a  $T^2$  power law but is still dominated by a  $T$ -linear term (see inset of Fig 2). In this context, the detailed study of Tl2201 with modern single particle spectroscopies would be extremely desirable, as it might provide direct insights into the nature of the

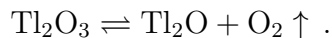
quasiparticles in both the normal and superconducting states [2, 3, 5].

Unfortunately, despite its great potential, progress on the Tl2201 system has been slow because of difficulties in the growth of single crystals. The thallium oxide is volatile, reactive, and highly toxic, a combination which places constraints on the crystal growth technique. Standard growth procedures such as flux-growth in open crucibles or the use of a floating zone image furnace would allow toxic vapors to escape into the lab and deplete the thallium in the reaction vessel by allowing it to sublime out in a colder part of the furnace. It is thus essential to contain the growth components within a non-reactive enclosure so that thallium is not lost through either reaction or evaporation.

In Section 2, we report on our effort in the growth of high-purity single crystals of Tl2201, by a copper-rich self-flux method, and in their careful annealing in a controlled oxygen atmosphere. We will show that this material can be cleaved to expose a clean and stable [001] surface suitable for single particle spectroscopy experiments, as was demonstrated by the first successful study of the Fermi surface and quasiparticle excitations of Tl2201 by ARPES [35]. The detailed results of our ARPES study of several doping levels will be presented in Section 3, and a discussion linked to other theoretical and experimental results will be given in Section 4. The quantitative agreement between the ARPES and AMRO [32] determined Fermi surfaces indicates that Tl2201 may be the ideal testing ground for finally joining together the modern single particle spectroscopies and a host of well-established bulk probes of metals and superconductors. In particular, Tl2201 might be the ideal cuprate for a broad-based study of the normal metal that may underlie the superconductor in the overdoped regime, providing an understandable anchor point in the phase diagram of the high-temperature superconductors.

## 2. Tl2201 Single-Crystal Preparation

Difficult to prepare even as a ceramic, Tl2201 is even more challenging to grow as a crystal. Tl2201 melts incongruently and its crystals are grown from the high temperature solution (melt) made of its components. Ideally, this melt would be decanted to reveal freestanding flux-free crystals. While this technique is commonly used for growth of complex oxide crystals, there are a few challenges particular to Tl2201 system. The difficulties are due to the thallium oxide precursor. Around 800°C, trivalent thallium oxide decomposes into a monovalent oxide and oxygen gas [36]:



While the oxygen gas evolved must be allowed to escape, this decomposition leads to a more serious problem: at growth temperatures, the monovalent oxide's vapor pressure is of the order of 0.1 atm, high enough to allow it to escape rapidly. If the  $\text{Tl}_2\text{O}$  gas leaves the crucible, however slowly, the composition of the melt will be at best time-varying and at worst quickly devoid of thallium. The volatility of  $\text{Tl}_2\text{O}$  can also make the subsequent annealing of the crystals difficult, as the crystal surface may slowly decompose at temperatures at which the oxygen atoms are mobile. There are

several procedures that may be employed to mitigate these problems, including using pre-reduced thallium precursors such as  $Tl_2Ba_2O_5$  [37], encapsulation [38], or very high oxygen partial pressures. A further issue is that  $Tl_2O$  is quite reactive, most notably reacting with the quartz often used for encapsulation and furnace tubes.

To date, only a handful of groups have grown crystals of Tl2201. Mackenzie's group, using a gold lid on their crucible as a barrier to diffusion, found they could only successfully obtain crystals within a  $2^\circ C$  by 2 minute window [39, 40]. Hasegawa et al. used reduced thallium precursors and an alumina high-pressure bomb to control thallium loss [41, 38]. Kolesnikov et al. [42, 43, 44] do not report any special precautions for controlling the loss of thallium. In our growth effort, as we will discuss in detail in Section 2.1, we developed a flexible sealing scheme that permits the oxygen to escape as it is evolved, while at the same time containing the  $Tl_2O$ .

A last crucial issue with the preparation of Tl2201 single crystals, alluded to above, is that the crystal surfaces can degrade during the oxygen post-annealing required to set the charge carrier content, and in turn the temperature of the superconducting phase transition. So far most work on annealing of Tl2201 has been carried out on ceramic samples [45], but annealing of single crystals, where surface damage is more obvious, has been less successful — only Mackenzie's group reported success [39]. As a result, many crystals studied to date have been unannealed, resulting in inhomogeneous oxygen content and broad transitions ( $\Delta T_c = 10 \sim 20 K$ ), which can obscure many features and add unnecessary disorder. As part of our growth effort, we have also carefully explored the annealing of Tl2201 single crystals, succeeding in the preparation of samples ranging from near optimal doping to very overdoped, while avoiding surface damage.

### 2.1. Single-Crystal Growth

For the crystal growth we employ a copper-rich self-flux technique using a barium and copper precursor,  $BaCuO_2$  powder that was prepared from 99.999% pure  $BaCO_3$  and 99.995% pure  $CuO$  by repeated calcining under flowing oxygen. The use of carbonate-free barium cuprate avoids both carbon poisoning from  $BaCO_3$  and the cation impurities that may be encountered if one employs  $BaO_2$ , which is only available at lower cation purity. Carbon contamination is of particular concern in this system because there are several known superconducting thallium-based oxycarbonates [46].

The barium cuprate powder was mixed with 99.99% pure  $Tl_2O_3$  to a final cation ratio of  $Tl:Ba:Cu = 1.05:1:1$  [47], then loaded into a 10 mL alumina crucible. The crucible was sealed using a gold lid fixed in place with a 1 kg weight. Employing this sealing scheme,  $O_2$  gas may still escape as  $Tl_2O_3$  decomposes, but the seal becomes very effective once the contents of the crucible equilibrate at the growth temperature, thus preventing significant loss of  $Tl_2O$  (as monitored by mass-loss measurements). The charge was heated rapidly ( $300^\circ C/h$ ) to  $935^\circ C$ , while flowing oxygen to flush out any escaping thallium oxide, and held for 12h to equilibrate. It was cooled at  $-0.5^\circ C/h$  to  $890^\circ C$ , then allowed to cool freely to room temperature. The oxygen gas flowing

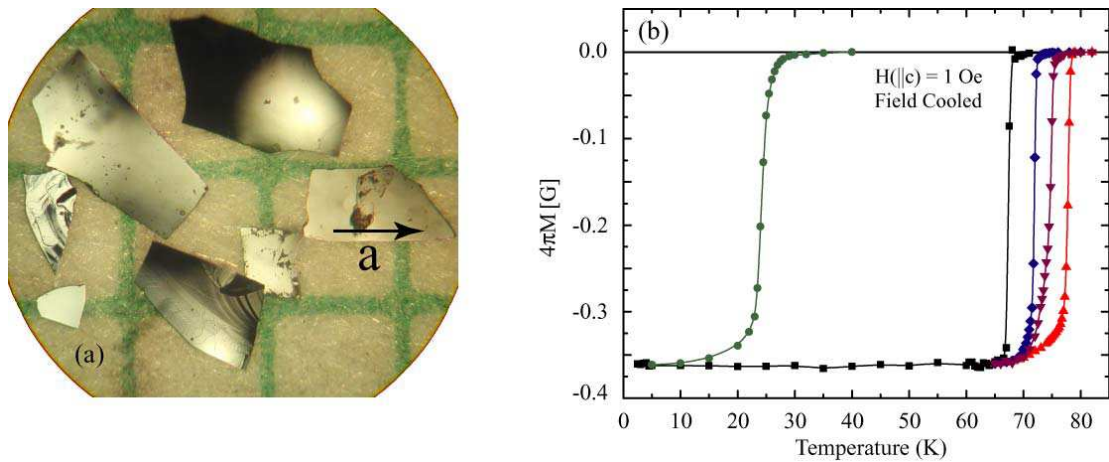


**Figure 3.** (a) Photo of several resulting Tl2201 crystals on millimeter graph paper; the orthorhombic *a*-axis of one crystal is marked. (b) Field-cooled magnetization curves for representative Tl2201 crystals annealed to different hole-doping levels; the sharpness of the superconducting transitions is an indication of the crystals' homogeneity.

through the furnace was bubbled through sulphuric acid and water to remove any thallium released during growth that did not condense in colder areas of the furnace. Most resulting crystals were embedded in flux, but free-standing platelet single crystals of  $1\sim 2\text{ mm}^2$  were harvested from voids in the flux ingot. As shown in Fig. 3(a), these crystals exhibited mirror surfaces with fine curved growth steps. All characterization and spectroscopy reported here was performed on flux-free, void-grown single crystals.

The as-grown samples typically have superconducting transitions of  $5\sim 10$  K (onset) and several Kelvins wide, a width comparable to other groups' as-grown samples. As-grown  $T_c$ s are determined by the cation substitution level, crystal dimensions, cooling rate, and the atmosphere around the crystals, the last two parameters being coupled through the equation of state for oxygen gas. Since as-grown superconducting transitions are typically quite broad and not homogeneous throughout the crystal, it is crucial that the crystals be annealed before they are studied. The crystals were annealed under controlled oxygen partial pressures at temperatures between  $290^\circ\text{C}$  and  $500^\circ\text{C}$ . This produces samples whose oxygen contents place them on the overdoped side of the phase diagram, with sharp superconducting transitions ranging from 5 to 85 K. We have not attempted to reach optimal doping, which in this system is believed to correspond to a superconducting  $T_c$  of at least 93 K [29], because even higher annealing temperatures would be required, increasing the risk of thallium loss.

## 2.2. Physical and Chemical Analysis

Since cation substitution can cause increased scattering, one objective of this work was to grow crystals with the lowest possible cation substitution level. Of more immediate importance than the reduction of cation defects, however, is reproducibility. Because cation substitution also dopes the crystal, variation between crystals would lead to

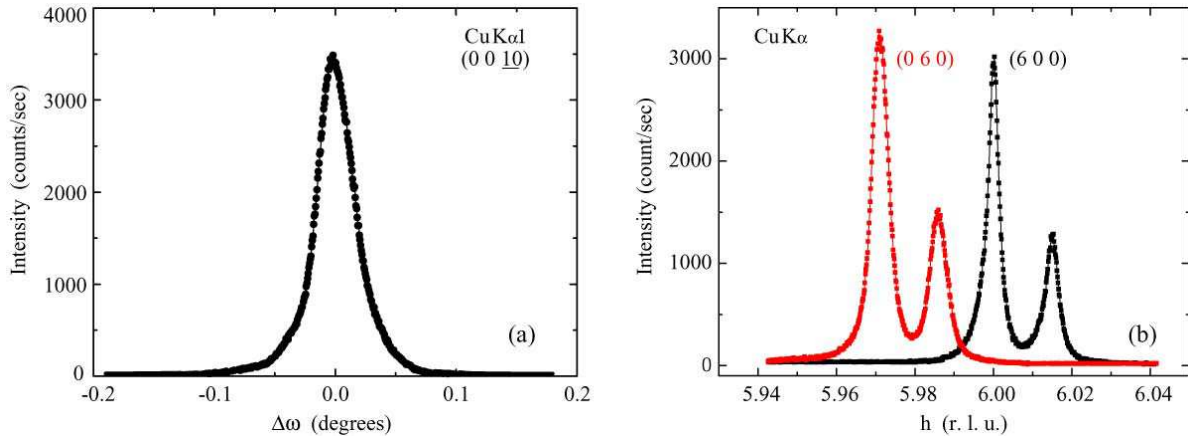


**Figure 4.** (a) The (0 0 10) rocking curve for a typical Tl2201 single crystal ( $T_c=67.7$  K); the FWHM is  $0.034^\circ$ , indicating excellent crystallinity. (b) The (6 0 0) and (0 6 0) peaks for a  $T_c=24$  K sample, showing the orthorhombicity of the crystal structure. The doublets correspond to CuK $\alpha_1$  and CuK $\alpha_2$  radiation results.

different  $T_c$ s as well as different scattering rates. More problematic still would be a variation within a crystal, which would arise from changes in the composition of the melt over the course of the crystal's growth. Although cation substitution is not desired and does dope the crystals, it must be emphasized that this is not used as a control parameter in doping these crystals. If the crystals can be grown with a reproducible level of cation substitution, the cation disorder will be the same for all dopings. This is in contrast to LSCO, where cation substitution is the primary control parameter, and must be varied by roughly a factor of four to traverse the superconducting dome.

To determine the levels of cation substitution in our crystals, electron-probe micro-analyses (EPMA) of several crystals were performed on a fully-automated CAMECA SX-50 instrument in wavelength-dispersion mode.‡ The cation composition (normalized to the barium content) was determined to be  $Tl_{1.884(6)}Ba_2Cu_{1.11(1)}O_{6+\delta}$  and was not observed to be position dependent on individual crystals, nor did it vary between crystals. This result corresponds to a level of copper substitution at the thallium site comparable to that reported previously [49, 39, 40, 44] for cation-substituted Tl2201. Al contamination was checked separately by EPMA and found to be below the 50 ppm detection limit, corroborating our observation that the crucibles were not corroded by the melt.§ Despite the cation non-stoichiometry, the high quality of these crystals is

‡ The EPMA was performed under the following operating conditions: excitation voltage, 15 kV; beam current, 20 nA; peak count time, 80 s; background count time, 40 s; and spot diameter, 10  $\mu$ m. Data reduction was performed using the “PAP”  $\varphi(\rho Z)$  method [48]. For the elements studied, the following standards, X-ray lines and monochromator crystals were used: elemental Tl, TlM $\alpha$ , PET; YBa<sub>2</sub>Cu<sub>3</sub>O<sub>6.920</sub>, BaL $\alpha$ , PET; and YBa<sub>2</sub>Cu<sub>3</sub>O<sub>6.920</sub>, CuK $\alpha$ , LIF. Tight Pulse Height Analysis (PHA) control was used to eliminate to the degree possible any interference from higher-order lines.

§ Operating conditions were the following: excitation voltage, 15 kV; beam current, 40 nA; peak count time, 500 s; background count time, 250 s; and spot diameter, 10  $\mu$ m. The matrix composition was fixed at stoichiometric; AlK $\alpha$  was standardized on  $\alpha$ -Al<sub>2</sub>O<sub>3</sub> using a TAP crystal monochromator.

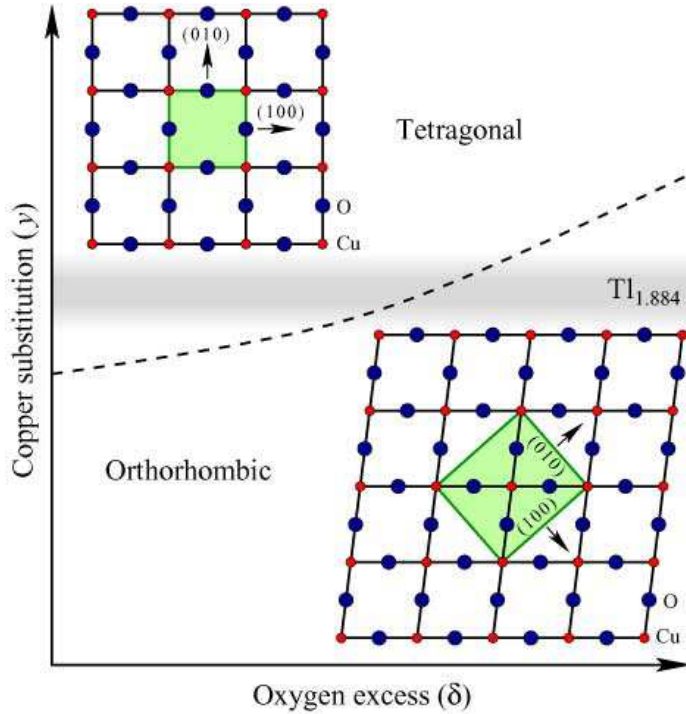


**Figure 5.** Schematic depiction of the dependence of the orthorhombic/tetragonal structural transition on  $y$  and  $\delta$  in  $Tl_{2-y}Ba_2Cu_{1+y}O_{6+\delta}$ . This scenario is suggested by the data from polycrystalline samples of Wagner et al. [29] and our own single crystal diffraction results (see Fig. 6). The  $CuO_2$  plane and unit cell (in green) are shown with and without the orthorhombic distortion, which is here exaggerated for clarity. The gray bar indicates where our crystals fall on this plot:  $y=0.116$ .

evidenced by their narrow superconducting transitions, measured by magnetization in a Quantum Design SQUID magnetometer (MPMS). Fig. 3(b) shows the field-cooled magnetization measured at 1 Oe ( $H \parallel c$ ), for crystals with transition widths (10%-90%) ranging from 4 to 0.7 K. The observed 40~60% Meissner fraction (i.e., fraction of flux excluded when cooling through  $T_c$ ) compares well with field-cooled results on other superconducting cuprates. It should also be mentioned that Tl2201's extremely low first critical field ( $H_{c1}$ ) makes the transitions appear broader in higher fields.

### 2.3. Structural Analysis: Crystallinity and Symmetry

To investigate the samples' crystallinity, X-ray diffraction spectra and rocking curves were taken on a BEDE model 200 double-crystal diffractometer with a Si(111) monochromator; the entire sample was illuminated by the X-ray beam. Fig. 4(a) depicts the (0 0 10) X-ray rocking curve of a  $0.5 \times 1.2 \text{ mm}^2$  crystal annealed to  $T_c=67.7 \text{ K}$ . While the FWHM of  $0.034^\circ$  is broader than the  $0.006^\circ$  obtained for the best  $YBa_2Cu_3O_{7-\delta}$  crystals grown in  $BaZrO_3$  crucibles, it is similar to the  $0.02\text{--}0.03^\circ$  achieved for  $YBa_2Cu_3O_{7-\delta}$  grown in YSZ crucibles [50], indicating a good degree of crystalline perfection. A crystal annealed to achieve a relatively high oxygen content

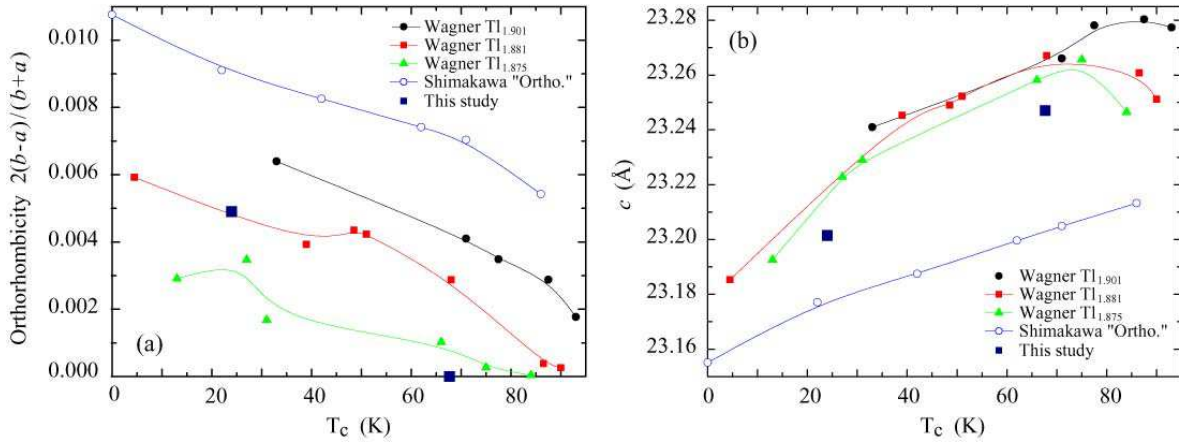


**Figure 6.** Comparison of the orthorhombicity between our crystals and Wagner's [29] and Shimakawa's [51] ceramics: orthorhombicity and  $c$ -axis lattice constant vs.  $T_c$ .

and strong overdoping ( $T_c=24$  K) was found to be orthorhombic with lattice parameters  $a=5.4580(3)$  Å,  $b=5.4848(5)$  Å and  $c=23.2014(5)$  Å, consistent with the lattice constants reported for ceramics with similar  $T_c$  and Cu substitution [29]. This orthorhombicity is determined by the x-ray diffraction data presented in Fig. 4(b): the two data sets were recorded independently for  $a$  and  $b$  axes and would be identical to one another if the crystals were tetragonal. Closer to optimal doping, and at a lower interstitial oxygen content, the  $T_c=67.7$  K sample was tetragonal to within our resolution

Tl2201's crystal symmetry depends on the level of cation substitution and the oxygen content. Stoichiometric and near-stoichiometric ceramics have been shown to be orthorhombic for all oxygen contents, while heavily-substituted ones are strictly tetragonal [51]. For intermediate levels of substitution, the orthorhombicity depends on the oxygen content: samples with higher oxygen contents are more orthorhombic [29]. The orthorhombic distortion is thought to arise from a lattice mismatch between the CuO<sub>2</sub> plane layer and the naturally larger Tl<sub>2</sub>O<sub>2</sub> double layer. Interstitial oxygens increase the distortion, while cation disorder seems to suppress it. The distortion and its dependence on the oxygen content  $\delta$  and the copper substitution  $y$  are shown schematically in Fig. 5. Powder X-ray diffraction shows that the orthorhombic distortion is an elongation along one plaquette diagonal, with the Cu-O bonds remaining the same in both directions. The distortion is quite minor: instead of being at right angles, the Cu-O bonds meet at  $\approx 89.7^\circ$  in orthorhombic samples. The plaquette diagonals, identified with nodes in the superconducting gap, remain orthogonal, so no mixing of order parameter symmetries is required. For these reasons and for ease of comparison with other systems, all ARPES analysis reported here is based on the original tetragonal unit cell, regardless of the actual symmetry of the crystals.

Our crystals' orthorhombicity, defined as  $2(b-a)/(b+a)$ , is consistent with that found by Wagner et al. [29] for similar levels of cation substitution, as shown in Fig. 6(a). One should keep in mind, however, that this quantity is highly prone to uncertainties

because of the smallness of the orthorhombic distortion, so that quantitative conclusions based on this graph should be treated with caution. Fig. 6(b) compares two of our annealed crystals' *c*-axis lattice parameters to the orthorhombic ceramic samples of Wagner et al. [29] and Shimakawa et al. [51]. Our *c*-axis lattice parameters are again similar to those of Wagner et al. [29], but we observe higher  $T_c$  values for the same lattice parameters (or a shorter *c* axis for the same  $T_c$ ). Possible explanations for this include improvements in  $T_c$  from higher homogeneity, cleaner samples or larger grain size (crystals vs. ceramics), more homogeneous annealing, or possibly a calibration disagreement between the diffractometers. Wagner's samples have transitions a few Kelvins wide, with long tails towards zero Kelvin, and  $T_c$  was defined using the 50% point, which may not be an accurate average of the bulk in such a situation.

### 3. The Low-Energy Electronic Structure of Tl2201

Angle-resolved photoemission spectroscopy (ARPES) is an important tool in the study of the electron dynamics in correlated-electron systems. Within the sudden approximation, it probes the energy and momentum dependence of the electronic excitation spectrum of an  $N - 1$  particle system, the so-called electron-removal portion of the single-particle spectral function  $A(\mathbf{k}, \omega)$  [5]. In the non-interacting picture, this spectral function consists of delta-function peaks located at the precise energy and momentum given by the band structure, i.e.  $A(\mathbf{k}, \omega) = \delta(\omega - \epsilon_{\mathbf{k}})$ . When interactions are considered, the single-particle spectral function is modified by the inclusion of the electron proper self energy  $\Sigma(\mathbf{k}, \omega) = \Sigma'(\mathbf{k}, \omega) + i\Sigma''(\mathbf{k}, \omega)$ , which captures all the of the many-body correlation effects. One can then write  $A(\mathbf{k}, \omega) = -\frac{1}{\pi} \frac{\Sigma''(\mathbf{k}, \omega)}{[\omega - \epsilon_{\mathbf{k}} - \Sigma'(\mathbf{k}, \omega)]^2 + [\Sigma''(\mathbf{k}, \omega)]^2}$ . With respect to the non-interacting case, the peaks in the spectral function shift in energy and gain a finite width, in a way dependent on the energy and momentum of the excitations. At those  $\omega$  and  $k$  for which the spectral function is still characterized by a single pole, energy and lifetime renormalization are directly described by  $\Sigma'(\mathbf{k}, \omega)$  and  $\Sigma''(\mathbf{k}, \omega)$ , respectively. The ARPES lineshape thus gives direct access to the lifetime of the excitation and can provide insights into the nature of the underlying interactions, for example whether or not electron-electron interactions are Fermi liquid-like, as discussed in relation to the Tl2201 transport data of Fig. 2. As it will be discussed in the following sections, the first successful ARPES experiments on Tl2201 have arrived at an agreement with bulk probes on key features such as the normal-state Fermi surface [32] and the superconducting gap [52]. This success suggests that detailed ARPES studies of Tl2201 have the potential to reveal the nature and strength of many-body correlations, upon approaching high- $T_c$  superconductivity from the more conventional overdoped regime.

#### 3.1. Band Structure Calculations

Since it is generally believed that the normal metal on the very overdoped side of the HTSC phase diagram can be described as a rather conventional Fermi liquid system, in

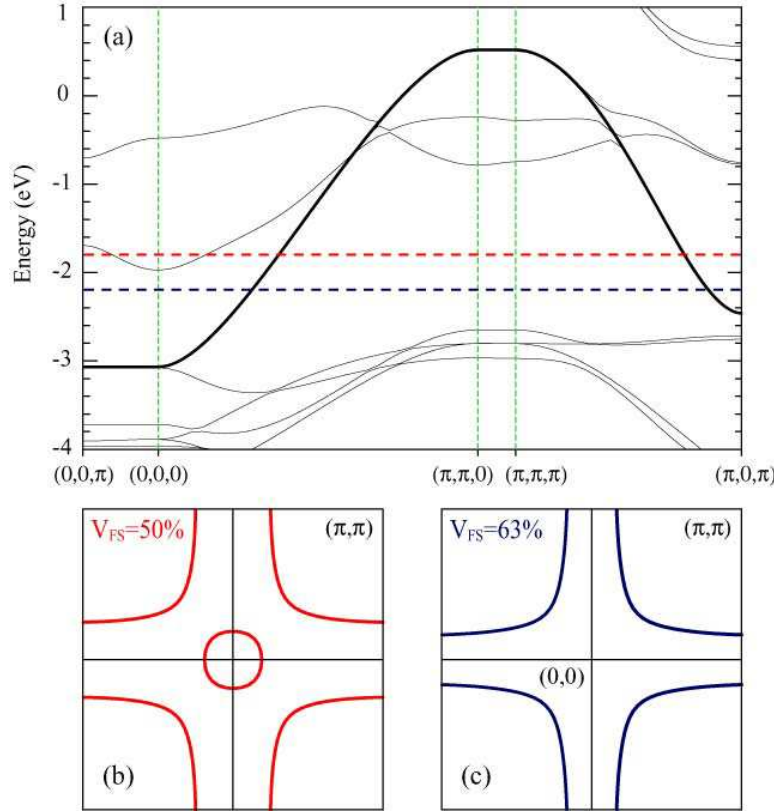


**Figure 7.** (a) Electronic dispersion obtained from band structure calculations within the local-density approximation (LDA). (b,c) Fermi surface calculated for two different doping levels enclosing a volume, counting holes, of 50% (orange) and 63% (blue) of the two-dimensional projected Brillouin zone; the corresponding position of the chemical potential with respect to the dispersive electronic bands is indicated in panel (a). Here, as in the rest of the paper,  $k$ -space labels are expressed modulo the lattice constants.

contrast to the strongly correlated Mott insulator found at half filling ( $p=0$  in Fig. 1), exploring the electronic structure and Fermi surface of heavily overdoped Tl2201 can start with the results of non-interacting band structure calculations performed within the local density approximation (LDA). As shown in Fig. 2 and especially Fig. 5, the most important structural element is the CuO<sub>2</sub> planes, which are well separated from each other by the TlO and BaO layers. As in all other HTSC cuprates, the CuO<sub>2</sub>-derived bands are expected to be the lowest energy electronic states and therefore directly determine the macroscopic electronic properties.

The results of band structure calculations along the high symmetry directions in the body-centered tetragonal Brillouin zone of Tl2201 are presented in Fig. 7(a). Coordinates for the atoms are taken from Ref. [53]. The essential low-energy feature of the band structure is indeed the highly dispersive Cu(3d<sub>x<sup>2</sup>-y<sup>2</sup></sub>)-O(1)(2p<sub>x,y</sub>) band; note however that this band is highly two-dimensional, with little dispersion along the  $k_z$  direction  $(0,0,k_z=0) \rightarrow (0,0,k_z=\pi)$ . Its top and bottom are located at  $(\pi,\pi)$  and  $(0,0)$ , respectively, within the two-dimensional projected Brillouin zone, while at  $(\pi,0)$  we find

the well-known van Hove singularity. The other two bands that sit at a comparable energy, i.e 0 to  $-2\text{ eV}$  in Fig. 7(a), are the anti-bonding  $\text{Tl}(6s)\text{-O}(2)\text{-O}(3)(p_z)$  bands, which do show significant dispersion in the  $k_z$  direction. Based on the formal valences of stoichiometric and undoped  $\text{Tl}_2\text{Ba}_2\text{CuO}_{6+\delta}$  (2:2:1:6 with  $\text{Tl}^{3+}$ ,  $\text{Ba}^{2+}$ ,  $\text{Cu}^{2+}$ ,  $\text{O}^{2-}$ ,  $\delta=0$ ), the Fermi energy would be located at the red line in Fig. 7(a), and both the CuO and TlO bands would cross  $E_f$ . This would result in a Fermi surface with hole pockets associated with the CuO band, and a small, spheroidal TlO electron pocket at the  $\Gamma = (0, 0)$  point, as in Fig. 7(b). This small electron pocket was originally proposed as a possible explanation for why undoped  $\text{Tl}_2\text{Ba}_2\text{CuO}_6$  does not show the Mott insulating behavior expected for materials with a half-filled  $3d_{x^2-y^2}$  CuO band, such as undoped  $\text{La}_2\text{CuO}_4$  [53]. However, the non-stoichiometry of our samples ( $\text{Tl}_{1.884(6)}\text{Ba}_2\text{Cu}_{1.11(1)}\text{O}_{6+\delta}$ , see Section 2.2) provides additional hole doping ( $\sim 0.14$  holes/formula unit) that would push the CuO band further away from half-filling, driving the TlO band above  $E_f$ . This shift would generate a Fermi surface consisting solely of a CuO hole pocket around  $(\pi, \pi)$  similar to the results shown in blue in Fig. 7(a,c), which were calculated to match the 63% volume observed by ARPES on our  $T_c = 30\text{ K}$  overdoped Tl2201 crystal [35]. Finally, it should be mentioned that if the effect of hole doping through interstitial oxygen were explicitly included in the calculations, the TlO bands would be pushed to much higher energies, beyond the rigid band picture [54]. The analogous effects of Pb substitution or excess oxygen in the Bi-O layers of Bi-cuprates has recently been used to account for the lack of Bi-O electron pockets around  $(\pi, 0)$  in those materials [55].

### 3.2. Electronic Dispersion and Fermi Surface by ARPES

Fig. 8(b) shows ARPES data<sup>||</sup> from a  $T_c = 30\text{ K}$  very overdoped Tl2201 sample (Tl2201-OD30) taken close to the  $(0,0)$ - $(\pi, \pi)$  direction in momentum space, the so-called “nodal” direction where the  $d$ -wave superconducting gap is zero. Each line in Fig. 8(b) is an energy distribution curve (EDC) from a given position in momentum space along the line marked as I in the Fermi surface plot of Fig. 8(a). These EDCs show a strongly dispersing quasiparticle peak, related to the  $3d_{x^2-y^2}$  CuO band, which emerges from the background at high binding energies and progressively sharpens as it disperses all the way to the Fermi energy  $E_F$ . Note that the term *quasiparticle* (QP) is used in a loose sense to identify a reasonably sharp dispersive peak, without specifying in detail how the peak should be interpreted in terms of specific models for correlation effects

<sup>||</sup> The ARPES experiments were carried out at the Swiss Light Source (SLS) on the Surface and Interface Spectroscopy Beamline [56, 57, 58] and at the Stanford Synchrotron Radiation Laboratory (SSRL) on Beamline 5-4, in both cases using a Scienta SES-2002 photoelectron spectrometer. At SLS, all measurements were performed with circularly polarized 59 eV photons, with energy and angular resolutions of approximately 24 meV and 0.2°; the data were acquired on a strongly overdoped sample with  $T_c = 30\text{ K}$  (Tl2201-OD30), and a lightly overdoped sample with  $T_c = 63\text{ K}$  (Tl2201-OD63). The samples were cleaved *in situ* at  $6 \times 10^{-11}$  torr and kept at 10 K throughout the measurements. At SSRL, all data were acquired at 28 eV with linearly polarized light and with energy and angular resolutions of 15 meV and 0.35°. The SSRL data were from lightly overdoped samples with  $T_c = 74\text{ K}$  (Tl2201-OD74), which were cleaved at  $3 \times 10^{-11}$  torr and temperature cycled between 10 and 85 K.

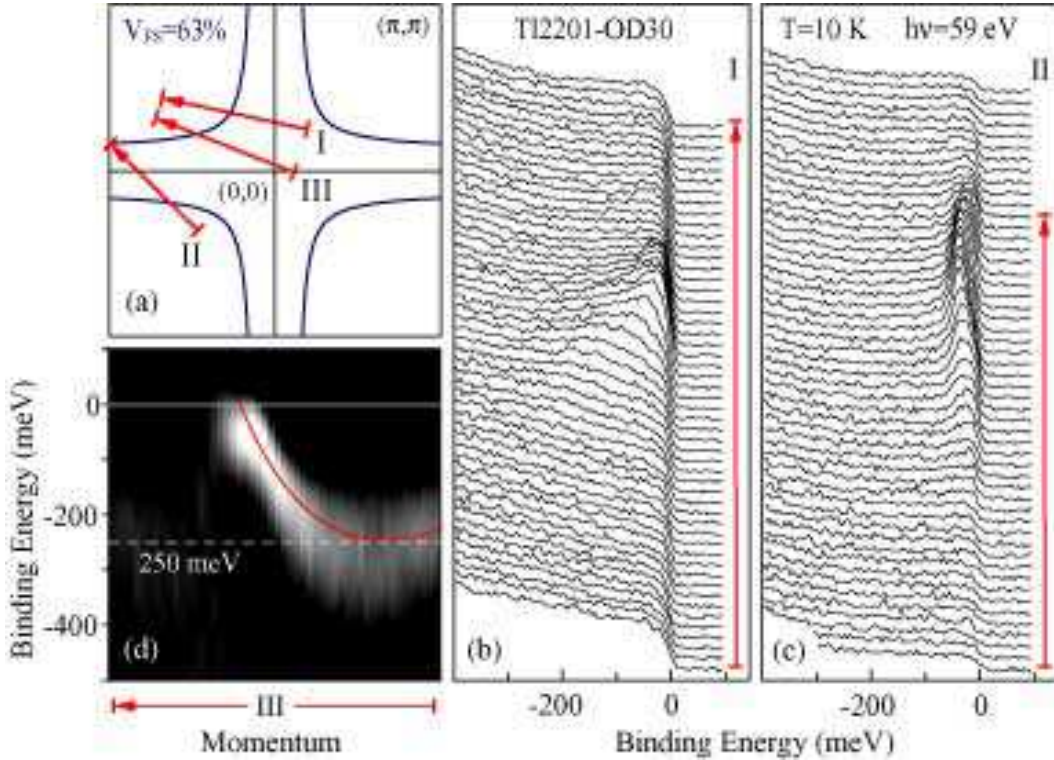


**Figure 8.** (a) Fermi surface calculated for a 63% Brillouin zone volume, counting holes, as in Fig. 7(c). (b,c) ARPES spectra taken at  $T = 10\text{ K}$  on Tl2201-OD30 along the directions marked by arrows I and II in (a). (d) Second derivative vs. energy of the spectra from along arrow III in (a); the red line is our tight-binding fit (see text).

(more discussion will be given in Sections 3.4 and 4). From the results of band structure calculations (Fig. 7), we expect the bottom of this band to be located at the  $\Gamma$  point, or  $(0,0)$ , at a binding energy of approximately 1 eV with respect to the chemical potential. Although it is hard to track the band all the way down to high binding energies in the raw data, it is possible to highlight the band dispersion by taking a second derivative of the ARPES intensity with respect to energy. This is plotted in Fig. 8d and indicates a filled bandwidth of only  $\sim 250\text{ meV}$ , suggesting a renormalization factor of about 4 between single particle band structure calculations and measured ARPES spectra.

Near  $(\pi,0)$ , the so-called “antinodal” direction where the  $d$ -wave superconducting gap exhibits its largest value, we also detected well-defined dispersive QP peaks, which define a shallow parabolic band. The bottom of this band corresponds to the extended van Hove singularity observed near  $(\pi,0)$  in all superconducting cuprates [2, 3]. However, at this high doping level, the van Hove singularity is located approximately 40 meV below the chemical potential. In comparison to the band structure calculations, this also shows a renormalization factor of about 5.

The momentum at which a dispersing QP peak is observed to reach  $E_F$  and disappear provides ARPES’s means of determining a Fermi wavevector  $k_F$ . This wavevector identifies one point along the normal state Fermi surface, which is the

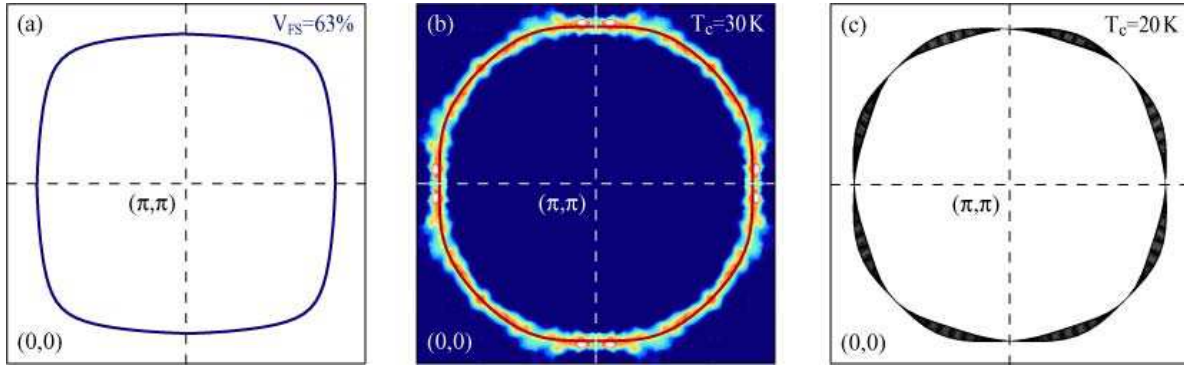


**Figure 9.** Fermi surfaces, in the projected two-dimensional Brillouin zone, obtained from: (a) band structure calculations (imposing a volume of 63% counting holes, as observed by ARPES on Tl2201-OD30); our (b) ARPES experiments on the  $T_c = 30\text{ K}$  sample (Tl2201-OD30); and (c) the AMRO study on a  $T_c = 20\text{ K}$  Tl2201 crystal by Hussey et al. [32]. The red line in (b) is the result of our tight-binding fit of ARPES Fermi surface and dispersion; the width of the Fermi surface contour in (c) reflects the magnitude of the  $c$ -axis dispersion, here emphasized by a factor of 4 for clarity [32].

contour in momentum space that separates filled from empty electronic states and whose existence and details are of fundamental importance for the understanding of the macroscopic physical properties of a material. By integrating the ARPES spectra over a  $\pm 5\text{ meV}$  energy window about  $E_F$  for a large number of cuts in momentum space and then plotting the results versus momentum in the two-dimensional projected tetragonal Brillouin zone, one obtains an estimate of the normal-state Fermi surface. This has been done for Tl2201-OD30, and is shown in Fig. 9(b). The location of the Fermi surface crossings has been determined over more than one quadrant across two different zones, and then downfolded to the first Brillouin zone and four-fold symmetrized to clearly show the detailed shape of the Fermi surface in the reduced zone scheme, with improved signal-to-noise. As expected, there is no indication of a TlO electron pocket around  $(0,0)$ . The Fermi surface determined from this procedure takes the form of a large hole pocket centered at  $(\pi,\pi)$  with an area that occupies  $63\pm2\%$  of the Brillouin zone, corresponding to a carrier concentration of  $1.26\pm0.04$  hole/Cu atom, or  $p=0.26\pm0.04$  greater hole density than the half-filled Mott insulator with 1 hole/Cu ( $p=0$  in Fig. 1). This result is in superb agreement with the recent study of the Fermi surface by angular dependence of magnetoresistance oscillations (AMRO) experiments [32], which found a hole-pocket volume of 62% of the Brillouin zone in a slightly more overdoped  $T_c = 20\text{ K}$  sample (Fig. 9(a)). The ARPES determination is also in good agreement with the estimates from low temperature measurements of the Hall coefficient, which gave a hole doping of  $p=1.30$  holes/Cu for a  $T_c \lesssim 15\text{ K}$  sample [33]. It is worth noting that the commonly used empirical formula,  $T_c/T_c^{max} = 1 - 82.6(p - 0.16)^2$ , which purports to connect the value of  $T_c$  to doping in a universal fashion [59], gives a much stronger dependence of  $T_c$  on doping than is shown by ARPES, AMRO, and Hall coefficient data. For our Tl2201-OD30 sample, from the above formula and the value  $p=0.26$  given by the Fermi surface

volume, one would obtain  $T_c \simeq 16$  K; and for the  $T_c = 15$  K sample studied by Mackenzie et al. [33], with the formula and the value  $p = 0.30$  determined from the Hall coefficient, one would actually get  $T_c = 0$  K. According to the empirical formula and contrary to what observed, Tl2201 should become non-superconducting already for  $p \simeq 0.27$ .

As a quantitative measure of the shape of the Fermi surface and of the many-body renormalized electronic dispersion, the Tl2201-OD30 ARPES data can be modelled by the tight-binding formula  $\epsilon_{\mathbf{k}} = \mu + \frac{t_1}{2}(\cos k_x + \cos k_y) + t_2 \cos k_x \cos k_y + \frac{t_3}{2}(\cos 2k_x + \cos 2k_y) + \frac{t_4}{2}(\cos 2k_x \cos k_y + \cos k_x \cos 2k_y) + t_5 \cos 2k_x \cos 2k_y$  [60], setting  $a = 1$  for the lattice constant. With parameters  $\mu = 0.2438$ ,  $t_1 = -0.725$ ,  $t_2 = 0.302$ ,  $t_3 = 0.0159$ ,  $t_4 = -0.0805$ ,  $t_5 = 0.0034$ , all expressed in eV, this dispersion reproduces both the Fermi surface shape, solid red line in Fig. 9(b), and the QP energy at  $(0,0)$  and  $(\pi,0)$ , as seen in Fig. 8(c,d). It is worth noting that experimentally the band bottom at  $(\pi,0)$  is extremely flat, a behavior that could not be reproduced by including only  $t_1$  and  $t_2$  hopping parameters in the model. Alternatively, a simple analytical formula for the three-dimensional electronic dispersion of Tl2201 has recently been derived, within the framework of the linear combination of atomic orbitals (LCAO) approximation, and was used to fit both ARPES and AMRO results [61]. A basis set spanning the Cu  $4s$ , Cu  $3d_{x^2-y^2}$ , O  $2p_x$  and O  $2p_y$  states was used in order to take into account the effective Cu-Cu hopping amplitude between Cu  $4s$  orbitals in neighboring CuO<sub>2</sub> layers. This approach emphasizes the significance of the Cu  $4s$  hopping amplitude in order to obtain the correct three-dimensional Fermi surface shape, an issue that was originally raised by Andersen *et al.* [62]. With regards to the detailed shape of the Fermi surface, LDA band structure calculations predict a more square contour than observed by ARPES and AMRO (Fig. 9(a)). The inclusion of correlation effects, as well as Cu-Tl substitution or interstitial O-doping beyond a rigid-band picture, might lead to a better agreement; preliminary attempts in this direction have not yet led to qualitative improvements [54].

### 3.3. ARPES Study of the Superconducting Gap

In order for Tl2201 to be a model system to study the overdoped HTSCs by surface and bulk sensitive probes, it is important to show that ARPES measures quantities that are characteristic of the bulk, for both normal and superconducting states. Therefore, in addition to the quantitative agreement on the normal state Fermi surface, the observance of a superconducting gap in agreement with bulk measurements is also a necessary requirement. In the following, we will discuss three different methods for the observation of a gap by ARPES. The first two show a gap consistent with a  $d_{x^2-y^2}$  form. The third method allows one to follow the temperature dependence of the gap, highlighting the minimal surface degradation that occurs as the temperature is cycled from 10 to 85 K.

The detection of a  $d_{x^2-y^2}$  gap using ARPES can be most easily visualized by the comparison of nodal and antinodal symmetrized spectra [64]. The spectra are symmetrized in energy about  $E_f$ , by taking  $I(\omega) + I(-\omega)$ , which minimizes the effects

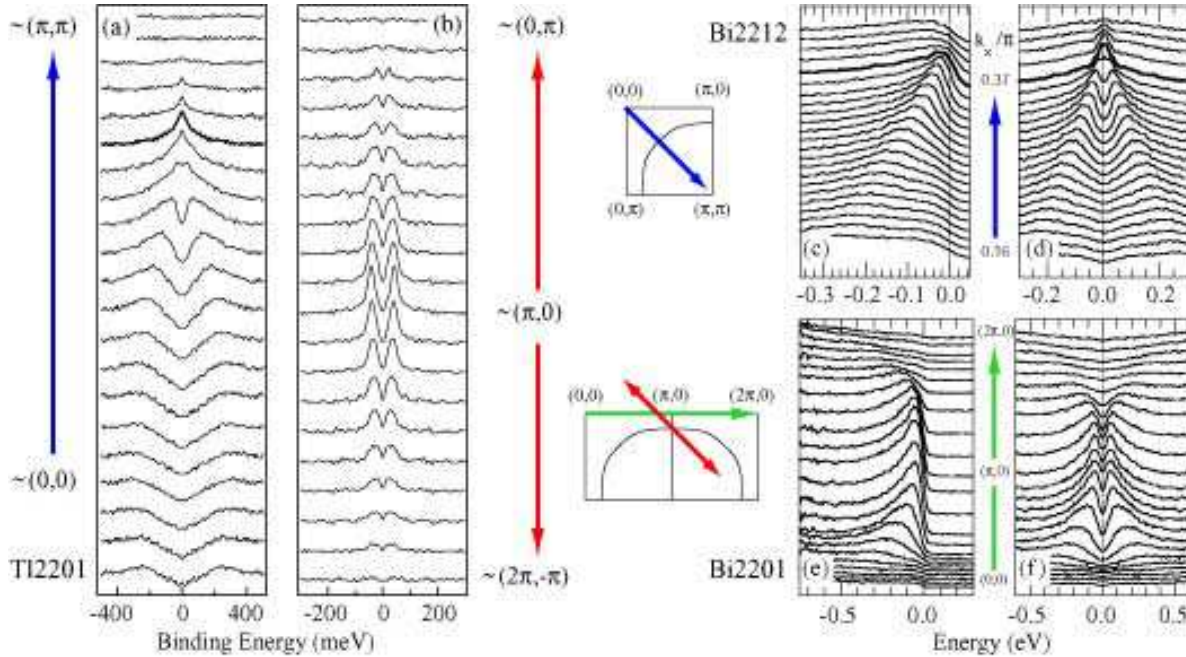


**Figure 10.** (a,b) Symmetrization of Tl2201-OD30 ARPES spectra from along cuts I and II in Fig. 8(b,c). ARPES spectra and their symmetrization along (c,d) the nodal direction for overdoped  $\text{Bi}_2\text{Sr}_2\text{CaCu}_2\text{O}_{8+\delta}$  ( $T_c = 88$  K), and (e,f) perpendicular to the antinodal direction for overdoped  $\text{Bi}_2\text{Sr}_2\text{CuO}_{6+\delta}$  ( $T_c = 23$  K); after Ref. [63]. For all samples, the approximate locations of the  $k$ -space cuts are indicated in the Brillouin zone sketches. Bold lines in (a,c,d) mark the spectra that cross the Fermi energy, identifying a Fermi wavevector  $k_F$ ; no crossing is observed for the spectra in (b,e,f).

of the Fermi function.¶ While this procedure does not return a quantitative value for the size of the superconducting gap, it provides a qualitative criterion for determining whether or not there is a Fermi crossing, and hence whether or not a superconducting gap has opened along the normal-state Fermi surface. In the symmetrized ARPES data, the presence of a peak in the spectra at  $E_F$  indicates the presence of a Fermi surface crossing. This procedure has been used extensively for the Bi-based cuprates, both single and bilayer compounds, in detailed investigations of the normal-state Fermi surface, as shown for instance in Fig. 10(c-f) [63], and of the superconducting as well as normal state pseudogap [64, 66]. In the case of our Tl2201-OD30 sample, this crossing is clearly seen in the nodal direction (bold line in Fig. 10(a)) but not in the antinodal direction (Fig. 10(b)), which is consistent with a  $d$ -wave functional form for the gap.

A more quantitative analysis of the gap can be performed by fitting ARPES spectra along cuts that cross the underlying normal-state Fermi surface, as shown in Fig. 11. The

¶ The symmetrization procedure assumes that the ARPES spectra are described by  $I(\omega) = f(\omega)A(\mathbf{k}, \omega)$ , and that there is particle-hole symmetry for a small range of  $\omega$  about  $E_F$  such that  $A(-\epsilon_{\mathbf{k}}, -\omega) = A(\epsilon_{\mathbf{k}}, \omega)$ . With the identity  $f(-\omega) = 1 - f(\omega)$ , it then follows that  $I(\omega) + I(-\omega) = A(\mathbf{k}, \omega)$ . It is worth pointing out that this procedure is not strictly valid in the case that energy and momentum resolutions are included in the description of  $I(\omega)$ , via convolution with the resolution function  $R(\Delta k, \Delta \omega)$ .

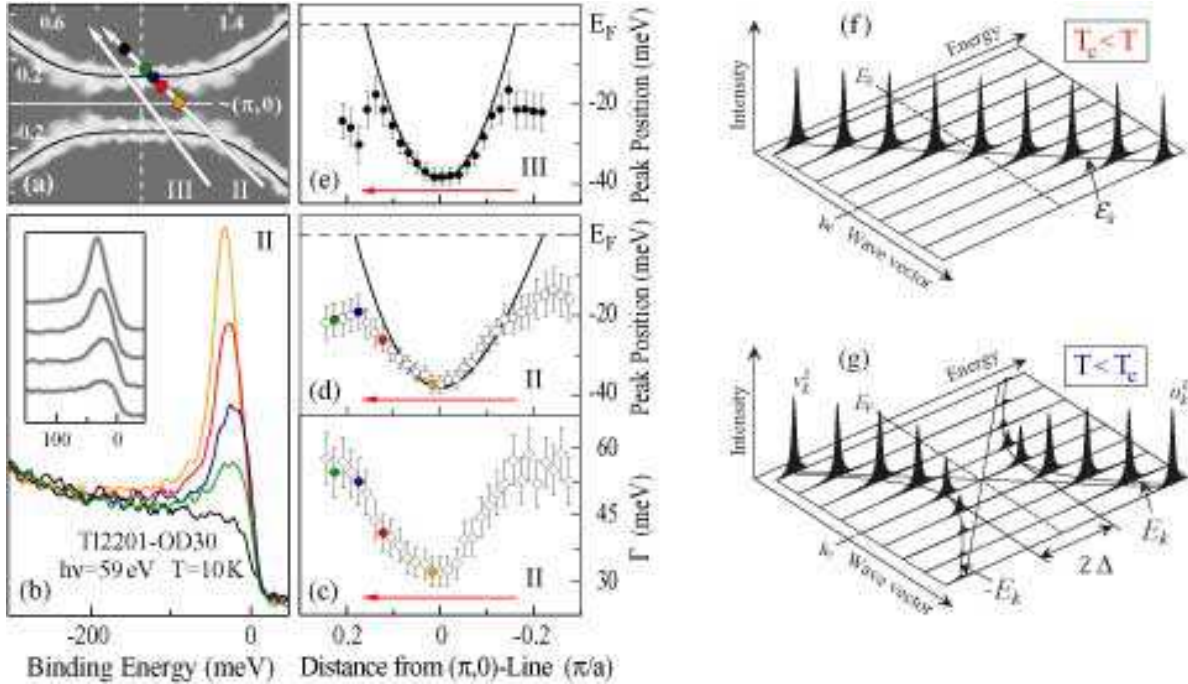


**Figure 11.** (a) Enlarged view of the Fermi surface of Tl2201-OD30 near  $(\pi, 0)$ . (b) Selected spectra from along cut II in (a); their  $k$ -space positions are indicated by circles of corresponding color. (c,d) QP linewidth  $\Gamma$  and peak position from a Lorentzian fit of the energy distribution curves along cut II in (a). (e) Similarly, QP peak position along cut III in (a). Black lines in (a,d,e) are our tight-binding results (see text). (f) Normal and (g) superconducting state single-particle spectral function, highlighting particle-hole mixing and backward dispersion of Bogoliubov QPs below  $T_c$  (after Ref. [65]).

model used to reproduce the spectra is a Lorentzian peak plus a step-like background. The latter is determined from the ARPES spectra with  $k \gg k_F$  and is used to help phenomenologically isolate the coherent part of the spectral function. This function is then multiplied by the Fermi function and convolved with the instrumental energy resolution function, to obtain the functional form to be fit to the data [2]. This procedure for determining the gap has been used previously for  $\text{Bi}_2\text{Sr}_2\text{CaCu}_2\text{O}_{8+\delta}$  [67]. The inset of Fig. 11(b) shows good agreement between the raw data and the fit. Since heavily overdoped cuprates have weaker, possibly Fermi liquid-like electron correlations, good agreement between the measured QP peak and the Lorentzian is in principle expected.

Fig. 11(d,e) show the peak positions from the fits compared with our tight-binding description of the normal-state electronic structure near the antinodal region. At higher binding energies, there is good agreement between the fit peak positions and the normal-state dispersion. At lower binding energies, however, the peak does not reach  $E_F$ , but instead reaches a minimum at  $\Delta_P \simeq 17$  meV and then disperses back to higher binding energy. This behavior is a hallmark of Bogoliubov QPs in a superconductor, as shown in the sketch of Fig. 11(f,g), for which a beautiful experimental demonstration was recently obtained by ARPES on the trilayer Bi-cuprate  $\text{Bi}_2\text{Sr}_2\text{Ca}_2\text{Cu}_3\text{O}_{10+\delta}$  [65]. Simultaneously,

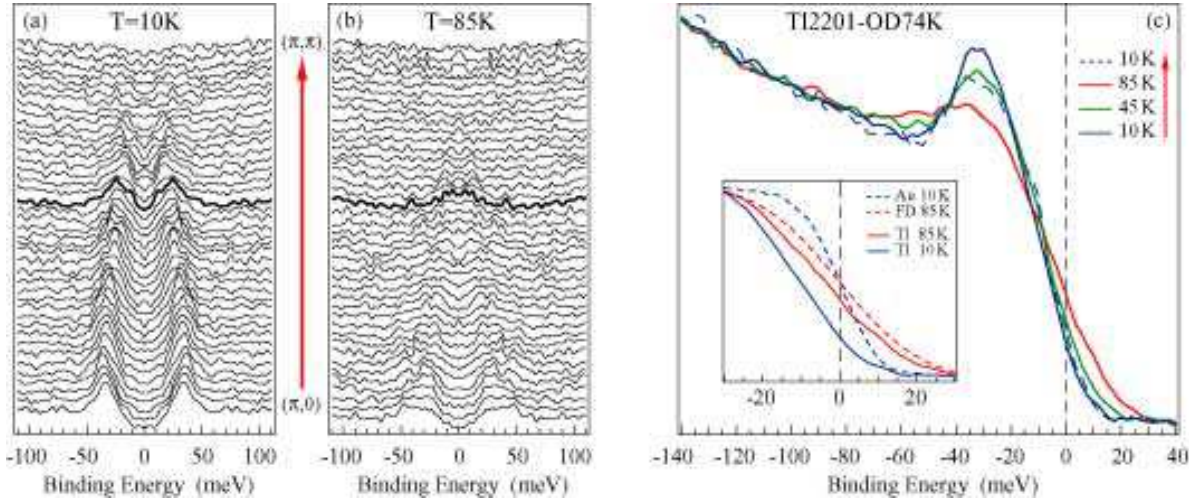


**Figure 12.** Symmetrized ARPES spectra measured at (a) 10 K and (b) 85 K on overdoped Tl2201-OD74, along the  $(\pi, 0) - (\pi, \pi)$  direction. Bold lines indicate the EDCs closest to  $k_F$ . (c) The  $k$  integrated spectral weight at the antinode, for several temperatures, together with a 10 K Au Fermi edge and an 85 K resolution-broadened Fermi function; an enlarged view of the leading edge positions is given in the inset.

we observe a reduction of spectral weight, by about a factor of 2, when the QP peak has dispersed from the van Hove singularity all the way to  $k_f$ . This is consistent with the spectral intensity of Bogoliubov QPs being determined by the coherence factor  $v_{\mathbf{k}}^2 = 1 - u_{\mathbf{k}}^2 = \frac{1}{2}(1 - \epsilon_{\mathbf{k}}/E_{\mathbf{k}})$ , with  $E_{\mathbf{k}} = \sqrt{\epsilon_{\mathbf{k}}^2 + \Delta_{\mathbf{k}}^2}$ , which corresponds to 1/2 when  $\epsilon_{\mathbf{k}} = \epsilon_{\mathbf{k}_f} = 0$  and 1 for  $|\epsilon_{\mathbf{k}}| \gg \Delta_{\mathbf{k}}$ . Extending this analysis to other momenta along the Fermi surface, one can study the  $k$ -dependence of the gap: at  $\sim(\pi/2, \pi/2)$  the peak does cross  $E_F$  (not shown), while at intermediate momenta a gap smaller than at  $(\pi, 0)$  is observed, as on the right-hand side of Fig. 11(d), consistent with  $d$ -wave symmetry.

The temperature dependence of the gap at the antinode has been measured for Tl2201-OD74. Fig. 12(a,b) present symmetrized ARPES data along the  $(\pi, 0) - (\pi, \pi)$  direction, at temperatures above and below  $T_c$ . In exactly the same manner as the  $k$ -dependent symmetrized data of Fig. 10(a,b), the temperature-dependent data of Fig. 12(a,b) show a clear gap at  $k = k_F$  at 10 K, which is clearly smaller at 85 K (with this type of analysis, the broadness of the QP peak and noise level at 85 K make it hard to conclude whether the gap has completely closed). Fig. 12(c) shows averaged EDCs taken over a narrow  $k$ -range around  $k_f$  at 10, 45, 85, and again at 10 K. Included in the figure is a 10 K Au reference spectrum, and the simulation of an energy-resolution broadened Fermi function at 85 K. The inset of Fig. 12(c) shows a closer view of these  $k$ -integrated EDCs around  $E_f$ . It is clear from this figure that, as the temperature increases, the size of the gap decreases although it does not seem to completely close at 85 K. This is suggested by comparing the position of the leading edge of the 85 K ARPES data with the simulated Fermi function; they are close in energy but not quite coincident. It is possible that there is still a pseudogap at temperatures slightly above

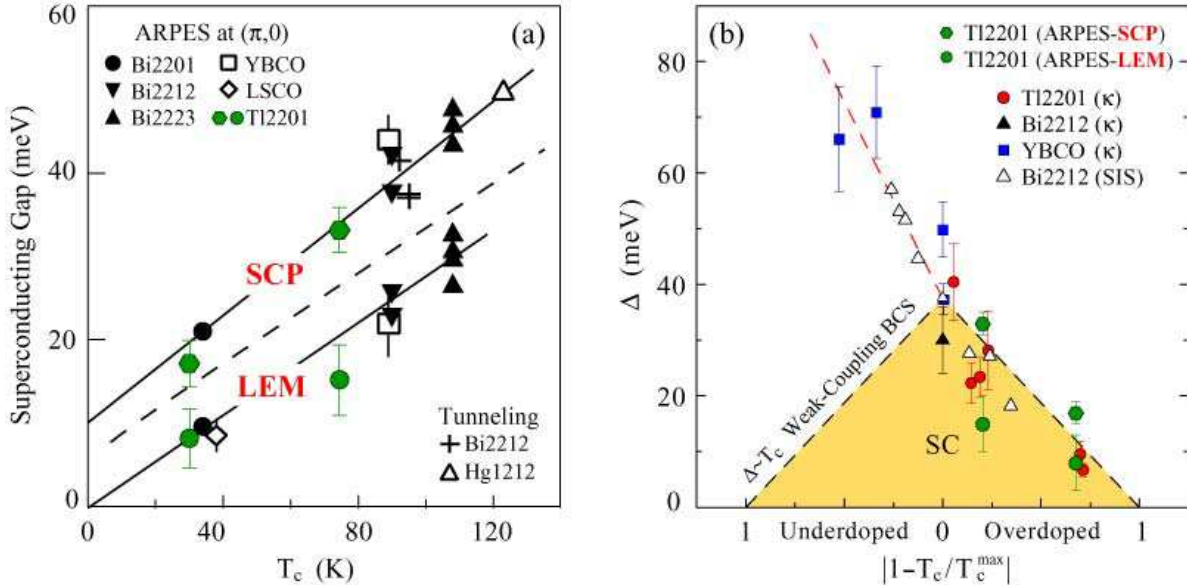


**Figure 13.** (a) Superconducting gap magnitude estimated by tunneling and ARPES from the superconducting peak position (SCP) and the leading-edge midpoint (LEM) shift, plotted versus  $T_c$  for various optimally or overdoped cuprates (after Ref. [68]). (b) Gap values from thermal conductivity, tunneling, and ARPES plotted vs.  $|1-T_c/T_c^{\max}|$  for many HTSCs across the phase diagram (after Ref. [52]); dashed lines are guides to the eye. Both plots include our own Tl2201-OD74 and Tl2201-OD30 ARPES data.

$T_c = 74$  K at this doping level. It is worth emphasizing that as the temperature is lowered back to 10 K, the gap reopens to approximately the same size. Although a partial degradation of the ARPES features can be seen, the QP peaks and the gap are still clearly observable. This is strong evidence that the surface is stable under these experimental conditions and is thus suitable for detailed surface-sensitive experiments. From these data, a superconducting peak (SCP) position of  $\sim 33$  meV and a leading-edge midpoint (LEM) gap of  $\sim 15$  meV can be extracted.

As a direct comparison with other cuprates and different means of determining the gap, Fig. 13(a,b) present a compilation of the doping dependence of the gap magnitude. Fig. 13(a) refers only to spectroscopic studies of optimally and overdoped HTSCs, for which the gap is proportional to  $T_c$ . Our results from Tl2201-OD74 and Tl2201-OD30 are fully consistent with the behavior observed on the other cuprates, as far as both SCP and LEM positions are concerned. Even more significant is Fig. 13(b), which demonstrates that ARPES measures gap values that follow the same trend as those derived from thermal conductivity, a bulk transport property. A more accurate comparison would require an analysis of the ARPES data beyond the mere determination of SCP and LEM positions, for instance on the basis of a model spectral function; this is however complicated by the non-trivial doping dependence of the ARPES data, and in the present case was done for Tl2201-OD30 but not Tl2201-OD74.

### 3.4. ARPES Lineshape Analysis

The electrical and thermal transport properties suggest that overdoped Tl2201 may be regarded as a Fermi liquid [33, 34, 32]. Since the ARPES data for both the normal and superconducting states indicate that single-particle surface-sensitive probes do provide information representative of the bulk, overdoped Tl2201 might be an ideal material for a quantitative study of the strength and nature of the many-body effects, which are revealed by the energy and momentum evolution of a QP's intrinsic ARPES lineshape [5]. In general, however, the shape of an ARPES peak does not correspond directly to an excitation's intrinsic lineshape. This is primarily due to an extrinsic contribution from momentum and energy resolution of the analyzer. Recent work on the model two-dimensional Fermi liquid system  $\text{Sr}_2\text{RuO}_4$  highlights the significant issues involved in removing the effects of the analyzer resolution [69]; in particular, it clearly shows that both the lineshape width and the peak position can be affected by resolution effects. There are significant challenges to completely removing the analyzer resolution from the data and stringent requirements on the data quality needed to attempt such analysis; therefore, we will analyze the current Tl2201 spectra in a more qualitative and phenomenological manner, concentrating primarily on the momentum dependence of the QP peaks measured in the superconducting state for different doping levels.

Beyond the issue of the experimental resolution, matrix element effects and the handling of the ARPES background are the two main complications in attempting even a qualitative description of the momentum dependence of the QP lineshapes. Experimentally, problems due to matrix element effects may be reduced by appropriate choice of measurement conditions such as geometry, photon energy, and polarization. For the experiments performed at the SLS and the data discussed in the following, circularly polarized 59 eV photons were used. Circular polarization was chosen specifically to minimize matrix element effects, which, using symmetry arguments, can be shown to be most extreme for linear polarization [2]. The photon energy was selected based on our experience on other cuprates — specifically,  $\text{La}_{2-x}\text{Sr}_x\text{CuO}_4$  (LSCO) where similar photon energies were used to reveal structure that had previously been missed in lower-energy ARPES data [70, 26]. Finally, in order to gain more reliable information, the ARPES data were taken over multiple Brillouin zones; this way it was possible to verify that, for the same point in the reduced zone scheme, the lineshapes from different zones in the extended zone scheme were qualitatively the same.

The most commonly used method to isolate a QP peak from the experimental background [2, 71], is to subtract a phenomenological ARPES background determined from the data at  $k$ -values far removed from those at which the QP-like peaks are detected. In our analysis we will use this approach, taking as background the weakly  $k$ -dependent photoemission intensity observed in each momentum space cut for  $k \gg k_F$ . The fundamental problem with this approach is that if some of the background is related to the incoherent part of the spectral function, as one would expect for correlated electron system, then by subtracting the background we are actually disregarding some

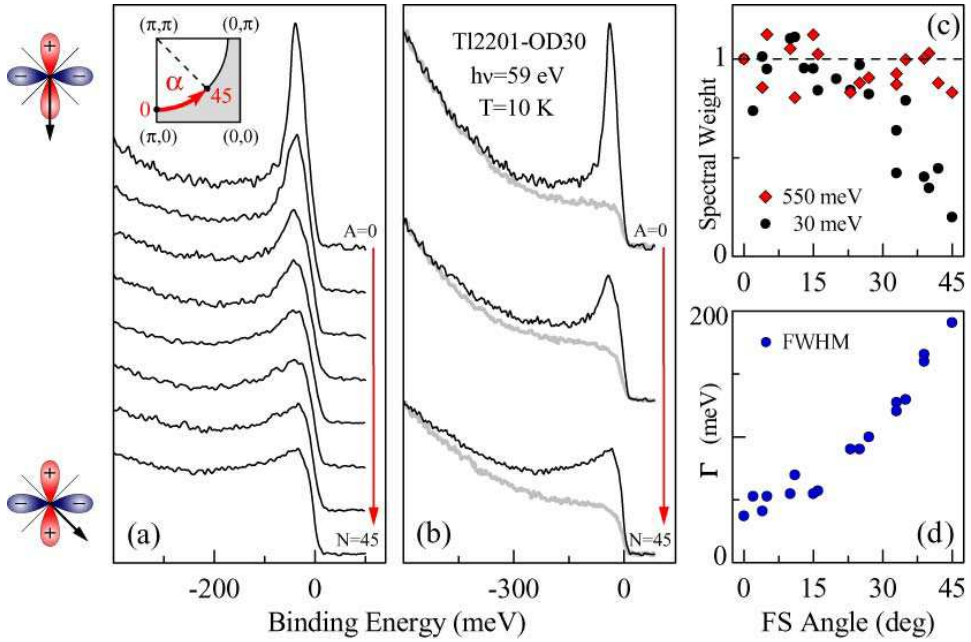


**Figure 14.** (a) Tl2201-OD30 ARPES spectra at  $k$  slightly smaller than  $k_F$  along the Fermi surface contour (corresponding to a QP binding energy of  $\sim 35$  meV). (b) Selected spectra from (a) along with their corresponding  $k \gg k_F$  background. (c) Spectral weight of the background subtracted spectra, integrated over different energy ranges and normalized with respect to the  $\alpha=0$  antinodal value, plotted vs. the Fermi-surface angle  $\alpha$ . (d) Quasiparticle linewidth  $\Gamma$  plotted vs. the Fermi-surface angle  $\alpha$ .

of the most crucial information contained in the ARPES spectra. In fact, the  $k$ - and  $\omega$ -dependence of the incoherent part of the spectral function is, in many respects, as important as the behavior of the QP peak itself; unfortunately we do not yet have the means to reliably extract information from it.

In Fig. 8(b), similar to what was previously observed in all photoemission studies of the cuprates [2, 3], we saw that in the nodal region the width of the QP peaks increases as a function of binding energy, as expected from simple phase-space arguments. This is, however, in sharp contrast to what is observed in the antinodal region, where the sharpest peak is found at the bottom of the band: in Fig. 11(c), the linewidth  $\Gamma$  of the QP peak is observed to grow from  $\sim 30$  to  $\sim 55$  meV as the QP peak disperses from  $\sim 39$  to  $\sim 20$  meV binding energy. Possible origins for this anomalous behavior will be discussed later, but it should be pointed out that an analogous effect was recently reported for very overdoped and nearly non-superconducting  $\text{Bi}_{1.74}\text{Pb}_{0.38}\text{Sr}_{1.88}\text{CuO}_{6+\delta}$  [72]. Another striking feature of the lineshape evolution is that the QP peaks are much broader in the *nodal* region than in the *antinodal* region, as evidenced by the direct comparison of Fig. 8(b) and 8(c). To elaborate on this, in Fig. 14(a) we present a compilation of spectra from along the Fermi surface contour, with  $k$  slightly smaller than  $k_F$  and corresponding to a binding energy of  $\sim 35$  meV. The choice in favor of spectral peaks at a binding energy

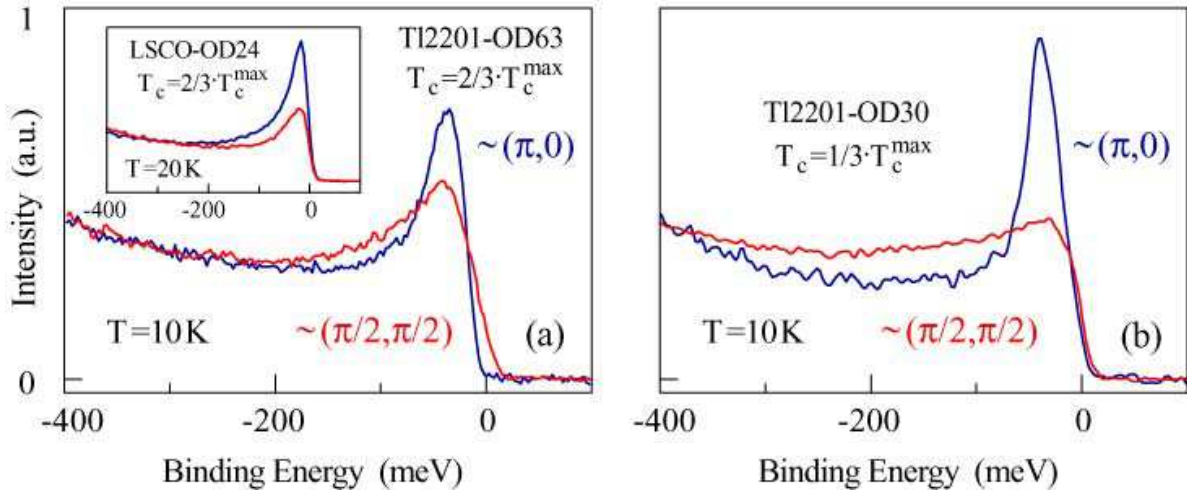


**Figure 15.** Nodal and antinodal spectra from (a) Tl2201-OD63 and (b) Tl2201-OD30, at  $k \lesssim k_F$ . Inset: similar data from overdoped LSCO-OD24 ( $p = 0.22$ ), from Ref. [73]. For both samples in (a),  $T_c \simeq \frac{2}{3} T_c^{\max}$  with respect to the  $T_c^{\max}$  of each family [27].

lower than  $E_F$  is dictated by the need to compare spectra not affected by either the opening of the  $d$ -wave gap or the anomalous low-binding-energy broadening seen at the antinode. The sharp peak near  $(\pi, 0)$  becomes progressively broader as  $(\pi/2, \pi/2)$  is approached. In order to determine whether this apparent broadening represents an increase in the QP linewidth  $\Gamma$ , or is merely a loss of spectral weight, the momentum-independent background from  $k \gg k_F$  is subtracted from the ARPES spectra as shown in Fig. 14(b); then the data are integrated over varying energy ranges and plotted in Fig. 14(c), normalized at the Fermi surface angle  $\alpha = 0^\circ$ . For narrow integration windows, there is a drop as a function of  $\alpha$ : the QPs show a loss of low-energy weight (and possibly coherence) in the nodal region. However, once the integration window is expanded to about 550 meV, the spectral weight of the QP peaks becomes angle-independent. This indicates that the  $k$ -dependent broadening of the ARPES spectra indeed reflects a loss of coherence of the QP spectrum, rather than being due to matrix element effects.

The observed QP anisotropy of Tl2201-OD30, with peaks much broader in the nodal than the antinodal region, is in sharp contrast to the behavior observed in underdoped cuprates, where the QP peaks are sharp near  $(\pi/2, \pi/2)$  and very broad around  $(\pi, 0)$ , as summarized in Fig. 17. As doping is increased, the antinodal QP peaks sharpen but remain significantly broader than the nodal QPs up to optimal doping, at least in the normal state. Even in the superconducting state, where antinodal QPs sharpen considerably, the ARPES linewidths for underdoped and optimally-doped materials are still highly anisotropic, with a minimum at  $(\pi/2, \pi/2)$  [2, 3]. Overall this behavior leads to the expectation that increasing doping beyond the optimal value will simply render the QP linewidths progressively more isotropic. Indeed, isotropic lineshapes were observed on early data from very overdoped, non-superconducting

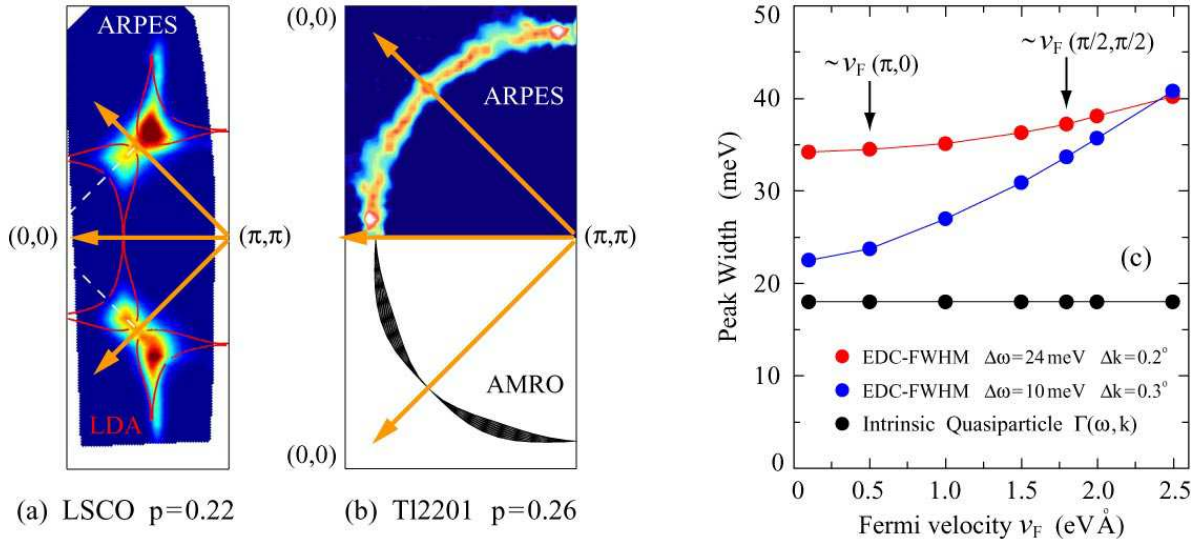


**Figure 16.** (a) ARPES intensity map for emission from the Fermi energy for overdoped LSCO-OD24 ( $p=0.22$ ). Red lines are the calculated LDA three-dimensional Fermi surface for  $k_z=0$  and  $\pi/c$ ; the enclosed area is the projection of the Fermi surface onto the two-dimensional  $k_x$ - $k_y$  plane, and denotes the region allowed for emission [74]. (b) ARPES and AMRO data from Tl2201-OD30. In (a,b) the yellow arrows identify directions characterized by zero  $k_z$  dispersion as indicated by the LDA calculations and consistent with AMRO experiments, which also suggest much weaker residual three-dimensionality effects in Tl2201 than in LSCO. (c) Resolution contributions to the width of an ARPES EDC calculated, as a function of the Fermi velocity  $v_F$ , from the two-dimensional convolution of a Lorentzian quasiparticle peak (binding energy  $\omega=30$  meV and intrinsic width  $\Gamma=18$  meV) with Gaussian energy and momentum resolution functions (results corresponding to our experimental parameters are in red).

$\text{Bi}_{1.80}\text{Pb}_{0.38}\text{Sr}_{2.01}\text{CuO}_{6-\delta}$  [75], although more recent work on the same material [72] exhibits a behavior more consistent with what is reported here for Tl2201. Going back to the QP anisotropy reversal observed for Tl2201-OD30 in Fig. 14, and presented again in Fig. 15(b) for nodal and antinodal points only, it must be emphasized that the same, albeit less pronounced, effect was observed in our Tl2201-OD63 sample, as shown in Fig. 15(a). For comparison, in the inset of Fig. 15(a) we have plotted ARPES data from overdoped ( $x=p=0.22$ )  $\text{La}_{2-x}\text{Sr}_x\text{CuO}_4$  [73]. This sample has  $T_c \simeq \frac{2}{3}T_c^{\max}$ , comparable to the degree of overdoping of our sample Tl2201-OD63, which also has  $T_c \simeq \frac{2}{3}T_c^{\max}$  for the much larger  $T_c^{\max}$  of the Tl2201 family. The data from LSCO exhibit a QP anisotropy similar to that in Tl2201-OD63, suggesting that the observed QP anisotropy reversal might indeed be generic to the overdoped cuprates.

Before proceeding to the discussion of the broader significance of these findings, we comment here on two extrinsic effects that could potentially contribute to an anomalous  $k$ -dependent broadening of the QP lineshapes: residual  $k_z$  electronic dispersion and resolution broadening effects. First, the dispersion of the electronic structure along the  $c$ -axis may indeed give rise to  $k_{||}$ -dependent broadening of the ARPES features [74]

(where  $k_{\parallel}$  is the  $ab$ -plane momentum). This effect could be doping-dependent because there is a 0.4%  $c$ -axis lattice constant reduction as doping is increased [29]. However, the  $k_z$ -dispersion vanishes in Tl2201 along the  $(0, 0) - (\pi, \pi)$  and  $(\pi, 0) - (\pi, \pi)$  directions, and thus at all nodal and antinodal points. This is a direct consequence of the symmetry of the body-centered tetragonal unit cell, and holds also for LSCO. Fig. 16(a,b) illustrate this point by showing ARPES data for both materials together with band structure calculations for LSCO [74], and AMRO data for Tl2201 [32]. Along these high-symmetry directions, no  $k_z$ -dispersion is present either in the LSCO calculations or the Tl2201 AMRO data (in both cases the  $k_z$ -dispersion is proportional to the width of the three to two-dimension projected contours). This is consistent with the ARPES maps for the two systems, although the broader  $E_F$  intensity patches for LSCO indicate that the three-dimensionality is much stronger in LSCO than in Tl2201. A residual  $k_z$  dispersion might contribute to the overall width of the ARPES features, but it cannot be responsible for the reversal of the anisotropy observed on overdoped cuprates, since the anisotropy exhibits a monotonic  $k_{\parallel}$ -dependence between  $(\pi/2, \pi/2)$  and  $\sim(\pi, 0)$ .

The second extrinsic effect that influences the width in energy of an ARPES spectrum, or EDC, is instrumental resolution. In a two-dimensional system, the width in energy is determined by the intrinsic inverse lifetime of the QP excitation and by the experimental resolution broadening, which reflects both the energy ( $\Delta\omega$ ) and angular ( $\Delta k$ ) resolution of the apparatus [5]. For a dispersionless feature, the instrumental contribution to the total EDC width is determined solely by the energy resolution  $\Delta\omega$ . However, for a dispersive feature, the angular resolution  $\Delta k$  contributes to the energy broadening in a manner directly proportional to the band velocity ( $v_F \neq 0$  in Fig. 16(c)). Since the Fermi velocity around the Fermi surface of the cuprates is highly anisotropic, varying from approximately 0.5 to 1.8 eV Å in going from antinodal to nodal region, this should give rise to a momentum-dependent resolution broadening of the EDCs. This broadening would be more severe at the nodes, where  $v_F$  is at its largest, which raises the concern that the larger nodal widths shown in Fig. 14 and 15 might be an artifact of the instrumental resolution. We have carefully evaluated the contribution of resolution broadening effects for our experimental conditions with a variety of different procedures and the results are summarized in Fig. 16(b). For our experimental parameters (red data,  $\Delta\omega = 24$  meV and  $\Delta k = 0.3^\circ$ ) the  $k$ -dependent resolution broadening is of the order of few meV, nowhere near the factor of 4 observed in Fig. 14(d).

#### 4. Discussion and Conclusions

Using a self-flux method and partial encapsulation, we have grown single crystals of the single-layer overdoped cuprate superconductor Tl2201. The crystals were annealed under controlled oxygen partial pressures to set a homogeneous doping level whilst preventing decomposition, and typically exhibited sub-Kelvin superconducting transition widths as measured in a SQUID magnetometer. Their high quality and homogeneity were evidenced not only by these narrow transition widths but also by

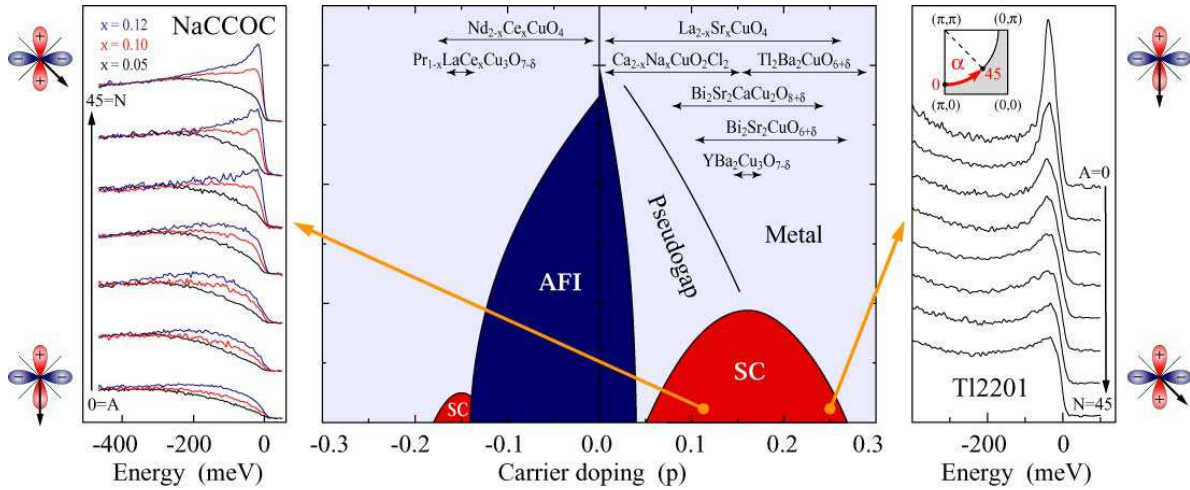


**Figure 17.** Nodal-antinodal quasiparticle anisotropy reversal observed in the cuprates. As a function of the Fermi surface angle  $\alpha$ , sharp QP peaks are observed at the nodes (N) and ill-defined QPs at the antinodes (A) in underdoped cuprates (e.g., data from  $\text{Ca}_{2-x}\text{Na}_x\text{CuO}_2\text{Cl}_2$ , after Ref. [10]); in overdoped Tl2201, this behavior is reversed.

their extremely narrow rocking curve widths, comparable to  $\text{YBa}_2\text{Cu}_3\text{O}_{7-\delta}$  grown in YSZ crucibles [50]. An EPMA study found the crystals to have the composition  $\text{Tl}_{1.884(6)}\text{Ba}_2\text{Cu}_{1.11(1)}\text{O}_{6+\delta}$ , which was homogeneous and was not observed to vary between crystals. This level of cation substitution is similar to that reported earlier for single crystals of Tl2201. For higher dopings (lower  $T_c$ s), the crystals were found to be orthorhombic, a slight deviation from a square-planar lattice that is often associated with the unsubstituted phase which has only been prepared in ceramics. The orthorhombic distortion appears to be suppressed by cation disorder, but stabilized by the oxygen interstitials that do increase the doping into the very overdoped regime.

While these crystals constitute a significant step forward, much optimization of the growth technique remains, and there is still the challenge of growing single crystals without the cation disorder in the Tl layer. Still, the high quality Tl2201 single crystals grown as part of this effort have enabled the first successful ARPES experiments of this compound. The results on the Fermi surface of Tl2201 mark an important new starting point for understanding the cuprates, namely that there is a material where both a surface-sensitive single-particle spectroscopic technique (ARPES) and comparable bulk transport measurements (AMRO) have arrived at quantitative agreement on a major feature of the normal state [32, 35]. This is a first for the copper-oxide high- $T_c$  superconductors and, within the more general class of 3d and 4d transition metal oxides, it is second only to the case of  $\text{Sr}_2\text{RuO}_4$  for which a similar quantitative agreement was reached between de Haas-van Alphen [76, 77] and ARPES [69, 78, 79, 80, 81]. The detailed agreement on the Fermi surface (Fig. 9), together with the good quantitative agreement achieved for the superconducting gap by thermal conductivity and ARPES (Fig. 13), establishes Tl2201 as an ideal system to study the overdoped regime of the

cuprate phase diagram with a wide spectrum of techniques. Next it will be important to study the single-particle excitation spectrum with both ARPES and STS in enough detail to compare to other normal state properties, thus critically testing whether or not a conventional Fermi-liquid description of the electronic properties captures the physics of the normal metal in the heavily overdoped regime. In this regard, it is important to elaborate on the most surprising result that emerged from this study of overdoped Tl2201 by ARPES, one which is counterintuitive within the realm of Fermi liquid theory: the quasiparticle anisotropy reversal observed across optimal doping. A summary of the momentum anisotropy in under and overdoped cuprates is given in Fig. 17, where data from  $\text{Ca}_{2-x}\text{Na}_x\text{CuO}_2\text{Cl}_2$  [10], for several doping levels, and Tl2201 are directly compared.

Early magnetotransport experiments on very overdoped Tl2201, for which a small magnetoresistance and a weak  $T$ -dependence of the resistivity and cotangent of the Hall angle have been observed, do not support the presence of strongly  $k$ -dependent low-temperature scattering rates in the normal state [33]. More recently, a temperature, doping, and magnetic field dependent AMRO study of Tl2201 suggested a two-component scattering rate consisting of an isotropic  $T^2$  term as well as an anisotropic  $T$ -linear term [82], which vanishes at the nodes and has a maximum near the antinodes. The anisotropic term becomes weaker upon overdoping the material, which is consistent with the view that as hole doping increases, the antinodal QPs should gain coherence faster than the nodal ones, eventually leading to a relatively small and fully isotropic scattering rate. Therefore, what is at variance between the ARPES and AMRO results from Tl2201 is not the behavior of the antinodal QPs, which in both cases are indeed gaining coherence upon overdoping, but rather that of nodal QPs which in ARPES become progressively less coherent. In addition, the overall magnitude of the scattering rate seen by ARPES is approximately a factor of 10 larger than estimated by AMRO.

What could be the origin for this discrepancy between ARPES and AMRO determined scattering rates? First of all, one has to note that while the ARPES experiments are performed in the superconducting state, the AMRO measurements are carried out in the normal state; and the latter is achieved by the application of external magnetic fields as high as 45T, which might potentially affect the low-energy QP dynamics. As for the reliability of the ARPES data on this specific point of the loss of coherence of nodal QPs at large dopings, it is important to mention that these findings are also supported by a preliminary study of overdoped  $\text{Bi}_2\text{Sr}_2\text{CaCu}_2\text{O}_{8+\delta}$  by STM and STS [83]. From the Fourier analysis of the energy-dependent spatial modulations observed in the tunneling conductance [84], it was concluded that for strongly overdoped samples, the nodal (i.e., low energy) quasiparticle interference signal is no longer visible, consistent with a decoherence of the nodal states [83].

A reconciliation of the results might require consideration of the specific sensitivity of transport probes and single-particle spectroscopies to electronic scattering phenomena. In particular, photoemission and scanning tunneling are very sensitive to electronic scattering involving small momentum transfer, while transport is rather insensitive to it. A possible source of such scattering could be extended impurities

far from the  $\text{CuO}_2$  planes [85], such as cation substitution or interstitial oxygen which increase with doping in most cuprates. Recent calculations show that the inclusion of elastic forward scattering in a  $d$ -wave superconductor can lead to an overall increase of the scattering rate in the normal state, but also to a strong enhancement of antinodal QP coherence in the superconducting state [86]. A very different model, based on the description of unitary-limit scattering beyond the Born approximation so as to account for multiple scattering from a single impurity, would also lead, below  $T_c$ , to loss of nodal coherence and anomalous enhancement of antinodal coherence [87]. However, both models predict an approximately isotropic QP scattering above  $T_c$ , as well as temperature dependent effects limited to the energy scale of the gap itself. To test the applicability of these scenarios to the present case, a thorough temperature dependent study is required. Finally, it should also be pointed out that sources of scattering relevant to this discussion are not just limited to impurities; also inelastic (i.e., electronic) scattering involving small momentum transfer might result in anomalous decoherence of the nodal QPs. For instance, low-energy (i.e., small  $q$ ) quantum-critical fluctuations associated with proximity to a competing superconducting  $d_{x^2-y^2} + id_{xy}$  phase [88], or ferromagnetic phases, could also lead to a similar QP anisotropy reversal [89].

## Acknowledgments

We gratefully acknowledge D.G. Hawthorn, K.M. Shen, N.E. Hussey, A.P. Mackenzie, J.C. Davis, D.J. Scalapino, and G.A. Sawatzky for discussions and M. Plat  , N.P. Armitage, A.B. Kuzmenko, S. Chiuzbaian, M. Shi, M. Falub, and L. Patthey for assistance during the ARPES experiments. We are also grateful to machine and beamline groups at the Swiss Light Source and Stanford Synchrotron Radiation Laboratory, whose outstanding efforts made the experiments possible. This work was supported by the Canada Research Chairs Program, the Natural Sciences and Engineering Research Council of Canada, the Canadian Institute for Advanced Research, and the British Columbia Synchrotron Institute.

## 5. References

- [1] March 2006, volume 2 no 3, special issue on high-temperature superconductors. *Nat. Phys.*, 2:133–210, 2006.
- [2] Andrea Damascelli, Zahid Hussain, and Zhi-Xun Shen. Angle-resolved photoemission studies of the cuprate superconductors. *Rev. Mod. Phys.*, 75:473–541, 2003.
- [3] J.C Campuzano, M.R. Norman, and M. Randeria. *Photoemission in the High  $T_c$  Superconductors*, volume II, pages 167–265. Springer, Berlin, 2004.
- [4]   ystein Fischer, Martin Kugler, Ivan Maggio-Aprile, Christophe Berthod, and Christoph Renner. *Rev. Mod. Phys.*, in press, 2006.
- [5] A. Damascelli. Probing the electronic structure of complex systems by ARPES. *Phys. Scr.*, T109:61–74, 2004.
- [6] C. Kim, P.J. White, Z.-X. Shen, T. Tohyama, Y. Shibata, S. Maekawa, B. O. Wells, Y. J. Kim, R. J. Birgeneau, and M. A. Kastner. Systematics of the photoemission spectral function of cuprates: insulators and hole- and electron-doped superconductors. *Phys. Rev. Lett.*, 80:4245–4248, 1998.

- [7] F. Ronning, C. Kim, K.M. Shen, N.P. Armitage, A. Damascelli, D.H. Lu, D.L. Feng, Z.-X. Shen, L.L. Miller, Y.-J. Kim, F. Chou, and I. Terasaki. Universality of the electronic structure from a half filled  $\text{CuO}_2$  plane. *Phys. Rev. B*, 67:035113, 2003.
- [8] K.M. Shen, F. Ronning, D.H. Lu, W.S. Lee, N.J.C. Ingle, W. Meevasana, F. Baumberger, A. Damascelli, N.P. Armitage, L.L. Miller, Y. Kohsaka, M. Azuma, M. Takano, H. Takagi, and Z.-X. Shen. Missing quasiparticles and the chemical potential puzzle in the doping evolution of the cuprate superconductors. *Phys. Rev. Lett.*, 93:267002, 2004.
- [9] T. Hanaguri, C. Lupien, Y. Kohsaka, D.H. Lee, M. Asuma, M. Takano, H. Takagi, and Z.-X. Shen. A ‘checkerboard’ electronic crystal state in lightly hole-doped  $\text{Ca}_{2-x}\text{Na}_x\text{CuO}_2\text{Cl}_2$ . *Nature*, 430:1001–1005, 2004.
- [10] Kyle M. Shen, F. Ronning, D.H. Lu, F. Baumberger, N.J.C. Ingle, W.S. Lee, W. Meevasana, Y. Kohsaka, M. Asuma, M. Takano, H. Takagi, and Z.-X. Shen. Nodal quasiparticles and antinodal charge ordering in  $\text{Ca}_{2-x}\text{Na}_x\text{CuO}_2\text{Cl}_2$ . *Science*, 307:901–904, 2005.
- [11] S. Smadici, P. Abbamonte, M. Taguchi, Y. Kohsaka, T. Sasagawa, M. Azuma, M. Takano, and H. Takagi. Absence of long-ranged charge order in  $\text{Na}_x\text{Ca}_{2-x}\text{CuO}_2\text{Cl}_2$  at  $x=0.08$ . *cond-mat/0603671*, 2006.
- [12] W.N. Hardy, D.A. Bonn, D.C. Morgan, R. Liang, and Kuan Zhang. Precision measurements of the temperature dependence of  $\lambda$  in  $\text{YBa}_2\text{Cu}_3\text{O}_{6.95}$ : Strong evidence for nodes in the gap function. *Phys. Rev. Lett.*, 70:3999–4002, 1993.
- [13] C.C. Tsuei and J.R. Kirtley. Pairing symmetry in cuprate superconductors. *Rev. Mod. Phys.*, 72:969–1016, October 2000.
- [14] J.R. Kirtley, C.C. Tsuei, A. Ariando, C.J.M. Verwijs, S. Harkema, and H. Hilgenkamp. Angle-resolved phase-sensitive determination of the in-plane gap symmetry in  $\text{YBa}_2\text{Cu}_3\text{O}_{7-\delta}$ . *Nat. Phys.*, 2:190–194, 2006.
- [15] D.A. Bonn and W.N. Hardy. *edited by D.M. Ginsberg*, chapter 2, page 7. in *Physical Properties of High Temperature Superconductors*. World Scientific, 1996.
- [16] R.W. Hill, Christian Lupien, M. Sutherland, Etienne Boaknin, D.G. Hawthorn, Cyril Proust, F. Ronning, Louis Taillefer, Ruixing Liang, D.A. Bonn, and W.N. Hardy. Transport in ultraclean  $\text{YBa}_2\text{Cu}_3\text{O}_7$ : Neither unitary nor Born impurity scattering. *Phys. Rev. Lett.*, 92:027001, 2004.
- [17] D.N. Basov and T. Timusk. Electrodynamics of high- $T_c$  superconductors. *Rev. Mod. Phys.*, 77:721–779, 2005.
- [18] T.P. Devereaux and R. Hackl. Inelastic light scattering from correlated electrons. *Rev. Mod. Phys. in press, cond-mat/0607554*, 2006.
- [19] M. Eschrig. The effect of collective spin-1 excitations on electronic spectra in high- $T_c$  superconductors. *Advances in Physics*, 55:47–183, 2006.
- [20] J.M. Tranquada. Neutron scattering studies of antiferromagnetic correlations in cuprates. *to be published as a chapter in Treatise of High Temperature Superconductivity, edited by J. Robert Schrieffer, cond-mat/0512115*, 2005.
- [21] D.J. Derro, E.W. Hudson, K.M. Lang, S.H. Pan, J.C. Davis, J.T. Markert, and A.L. de Lozanne. Nanoscale one-dimensional scattering resonances in the CuO chains of  $\text{YBa}_2\text{Cu}_3\text{O}_{6+x}$ . *Phys. Rev. Lett.*, 88:097002, 2002.
- [22] M.C. Schabel, C.-H. Park, H. Matsuura, Z.-X. Shen, D.A. Bonn, Ruixing Liang, and W.N. Hardy. Angle-resolved photoemission on untwinned  $\text{YBa}_2\text{Cu}_3\text{O}_{6.95}$ . I. Electronic structure and dispersion relations of surface and bulk bands. *Phys. Rev. B*, 57:6090, 1998.
- [23] D.H. Lu, D.L. Feng, N.P. Armitage, K.M. Shen, A. Damascelli, C. Kim, F. Ronning, Z.-X. Shen, D.A. Bonn, R. Liang, W.N. Hardy, A.I. Rykov, and S. Tajima. Superconducting gap and strong in-plane anisotropy in untwinned  $\text{YBa}_2\text{Cu}_3\text{O}_{7-\delta}$ . *Phys. Rev. Lett.*, 86:4370–4373, 2001.
- [24] S.V. Borisenko, A.A. Kordyuk, V. Zabolotnyy, J. Geck, D. Inosov, A. Koitzsch, J. Fink, M. Knupfer, B. Bchner, V. Hinkov, C.T. Lin, B. Keimer, T. Wolf, S.G. Chiuzbian, L. Patthey, and R. Follath. Kinks, nodal bilayer splitting, and interband scattering in  $\text{YBa}_2\text{Cu}_3\text{O}_{6+x}$ . *Phys. Rev. Lett.*, 96:117004, 2006.

- [25] I. Maggio-Aprile, Ch. Renner, A. Erb, E. Walker, and Ø. Fischer. Direct vortex lattice imaging and tunneling spectroscopy of flux lines on  $\text{YBa}_2\text{Cu}_3\text{O}_{7-\delta}$ . *Phys. Rev. Lett.*, 75:2754–2757, 1995.
- [26] X.J. Zhou, T. Cuk, T. Devreux, N. Nagaosa, and Z.-X. Shen. Angle-resolved photoemission spectroscopy on electronic structure and electron-phonon coupling in cuprate superconductors. *to be published as a chapter in Treatise of High Temperature Superconductivity, edited by J. Robert Schrieffer, cond-mat/0604284*, 2006.
- [27] H. Eisaki, N. Kaneko, D.L. Feng, A. Damascelli, P.K. Mang, K.M. Shen, Z.-X. Shen, and M. Geven. Effect of chemical inhomogeneity in bismuth-based copper oxide superconductors. *Phys. Rev. B*, 69:064512, 2004.
- [28] M. Chaio, R.W. Hill, C. Lupien, L. Taillefer, P. Lambert, R. Gagnon, and P. Fournier. Low-energy quasiparticles in cuprate superconductors: A quantitative analysis. *Phys. Rev. B*, 62:3554–3558, 2000.
- [29] J.L. Wagner, O. Chmaissem, J.D. Jorgensen, D.G. Hinks, P.G. Radaelli, B.A. Hunter, and W.R. Jensen. Multiple defects in overdoped  $\text{Tl}_2\text{Ba}_2\text{CuO}_{6+\delta}$ : Effects on structure and superconductivity. *Physica C*, 277:170–182, 1997.
- [30] C.C. Tsuei, J.R. Kirtley, Z.F. Ren, J.H. Wang, H. Raffy, and Z.Z. Li. Pure  $d_{x^2-y^2}$  order-parameter symmetry in the tetragonal superconductor  $\text{Tl}_2\text{Ba}_2\text{CuO}_{6+\delta}$ . *Nature*, 387:481–483, 1997.
- [31] H. He, P. Bourges, Y. Sidis, C. Ulrich, L.P. Regnault, S. Pailhes, N.S. Berzingerova, N.N. Kolesnikov, and B. Keimer. Magnetic resonant mode in the single-layer high-temperature superconductor  $\text{Tl}_2\text{Ba}_2\text{CuO}_{6+\delta}$ . *Science*, 295:1045–1047, 2002.
- [32] N.E. Hussey, M. Abdel-Jawad, A. Carrington, A.P. Mackenzie, and L. Ballcas. A coherent three-dimensional Fermi surface in a high-transition-temperature superconductor. *Nature*, 425:814–817, 2003.
- [33] A.P. Mackenzie, S.R. Julian, D.C. Sinclair, and C.T. Lin. Normal-state magnetotransport in superconducting  $\text{Tl}_2\text{Ba}_2\text{CuO}_{6+\delta}$  to millikelvin temperatures. *Phys. Rev. B*, 53:5848–5855, 1996.
- [34] Cyril Proust, Etienne Boaknin, R.W. Hill, Louis Taillefer, and A.P. Mackenzie. Heat transport in a strongly overdoped cuprate: Fermi liquid and a pure  $d$ -wave BCS superconductor. *Phys. Rev. Lett.*, 89:147003, 2002.
- [35] M. Platé, J.D.F. Mottershead, I.S. Elfimov, D.C. Peets, R. Liang, D.A. Bonn, W.N. Hardy, S. Chiuzbaian, M. Falub, M. Shi, L. Patthey, and A. Damascelli. Fermi surface and quasiparticle excitations of overdoped Tl2201 by ARPES. *Phys. Rev. Lett.*, 95:077001, 2005.
- [36] M.P. Siegal, E.L. Venturini, B. Morosin, and T.L. Aselage. Synthesis and properties of Tl–Ba–Ca–Cu–O superconductors. *J. Mater. Res.*, 12:2825–2854, 1997.
- [37] T.K. Jondo, R. Abraham, M.T. Cohen-Adad, and J.L. Jorda. The BaO–TlO<sub>1.5</sub> system. *J. Alloys Compd.*, 186:347–359, 1992.
- [38] Masashi Hasegawa, Humihiko Takei, K. Izawa, and Y. Matsuda. Crystal growth techniques for Tl-based cuprate superconductors. *J. Cryst. Growth*, 229:401–404, 2001.
- [39] André Tyler. *An Investigation into the Magnetotransport Properties of Layered Superconducting Perovskites*. Ph.D. thesis, University of Cambridge, 1998.
- [40] R.S. Liu, S.D. Hughes, R.J. Angel, T.P. Hackwell, A.P. Mackenzie, and P.P. Edwards. Crystal structure and cation stoichiometry of superconducting  $\text{Tl}_2\text{Ba}_2\text{CuO}_{6+\delta}$  single crystals. *Physica C*, 198:203–208, 1992.
- [41] Masashi Hasegawa, Yoshitaka Matsushita, Yasuhiro Iye, and Humihiko Takei. Growth and anisotropic superconducting properties of  $\text{Tl}_2\text{Ba}_2\text{CuO}_6$  and  $\text{Tl}_2\text{Ba}_2\text{CaCu}_2\text{O}_8$  single crystals. *Physica C*, 231:161–166, 1994.
- [42] N.N. Kolesnikov, M.P. Kulakov, V.N. Molchanov, I.F. Schegolev, R.P. Shibaeva, V.I. Simonov, R.A. Tamazyan, and O.M. Vyasilev. Comparative study of Tl-2201 single crystals with  $T_c = 30$  and 110 K by means of X-ray structural analysis and NMR. *Physica C*, 242:385–392, 1995.
- [43] O.M. Vyasilev, N.N. Kolesnikov, M.P. Kulakov, and I.F. Schegolev. Tl NMR study of  $\text{Tl}_2\text{Ba}_2\text{CuO}_x$  single crystals with various  $T_c$ . *Physica C*, 199:50–58, 1992.

- [44] N.N. Kolesnikov, V.E. Korotkov, M.P. Kulakov, V.N. Molchanov, R.A. Tamazyan, and V.I. Simonov. Structure of superconducting single crystals of 2201 thallium cuprate  $(\text{Tl}_{1.85}\text{Cu}_{0.15})\text{Ba}_2\text{CuO}_6$ ,  $T_c = 110$  K. *Physica C*, 195:219–224, 1992.
- [45] C. Opagiste, G. Triscone, M. Couach, T.K. Jondo, J.-L. Jorda, A. Junod, A.F. Khoder, and J. Muller. Phase diagram of the  $\text{Tl}_2\text{Ba}_2\text{CuO}_6$  compounds in the  $T$ ,  $p(\text{O}_2)$  plane. *Physica C*, 213:17–25, 1993.
- [46] B. Raveau, C. Michel, B. Mercey, J.F. Hamet, and M. Hervieu. Crystal chemistry of superconducting copper oxycarbonates. *J. Alloys Compd.*, 229:134, 1995.
- [47] J.L. Jorda, T.K. Jondo, R. Abraham, M.T. Cohen-Adad, C. Opagiste, M. Couach, A. Khoder, and F. Sibieude. Preparation of pure  $\text{Tl}_2\text{Ba}_2\text{CuO}_{6\pm\delta}$ : The contribution of phase equilibrium studies. *Physica C*, 205:177–185, 1993.
- [48] J.L. Pouchou and F. Pichoir. “PAP”  $\varphi(\rho Z)$  Procedure for Improved Quantitative Microanalysis, pages 104–106. San Francisco Press, 1985.
- [49] Y. Shimakawa, Y. Kubo, T. Manako, and H. Igarashi. Neutron-diffraction study of  $\text{Tl}_2\text{Ba}_2\text{CuO}_{6+\delta}$  with various  $T_c$ ’s from 0 to 73 K. *Phys. Rev. B*, 42:10165–10171, 1990.
- [50] Ruixing Liang, D.A. Bonn, and W.N. Hardy. Growth of high-quality YBCO single crystals using  $\text{BaZrO}_3$  crucibles. *Physica C*, 304:105–111, 1998.
- [51] Y. Shimakawa. Chemical and structural study of tetragonal and orthorhombic  $\text{Tl}_2\text{Ba}_2\text{CuO}_6$ . *Physica C*, 204:247–261, 1993.
- [52] D.G. Hawthorn, S.Y. Li, M. Sutherland, E. Boaknin, R.W. Hill, C. Proust, F. Ronning, M.A. Tanatar, J. Paglione, D. Peets, R. Liang, D.A. Bonn, W.N. Hardy, N.N. Kolesnikov, and L. Taillefer. The quasiparticle gap in  $\text{Tl}_2\text{Ba}_2\text{CuO}_{6+\delta}$  from low-temperature thermal conductivity. *Phys. Rev. B* in press, *cond-mat/0502273*, 2006.
- [53] David J. Singh and Warren E. Pickett. Electronic characteristics of  $\text{Tl}_2\text{Ba}_2\text{CuO}_6$ –Fermi surface, positron wavefunction, electric field gradients, and transport parameters. *Physica C*, 203:193–202, 1992.
- [54] S. Sahrakorpi, H. Lin, R.S. Markiewicz, and A. Bansil. Effect of hole doping on the electronic structure of Tl2201. *cond-mat/0607132*, 2006.
- [55] Hsin Lin, S. Sahrakorpi, R.S. Markiewicz, and A. Bansil. Raising Bi-O bands above the Fermi energy level of hole-doped  $\text{Bi}_2\text{Sr}_2\text{CaCu}_2\text{O}_{8+\delta}$  and other cuprate superconductors. *Phys. Rev. Lett.*, 96:097001, 2006.
- [56] T. Schmidt et al. *Nucl. Instrum. Methods Phys. Res., Sect. A*, 467-468:126–129, 2001.
- [57] U. Fleshig et al. *Nucl. Instrum. Methods Phys. Res., Sect. A*, 467-468:497–481, 2001.
- [58] See also <http://sls.web.psi.ch/view.php/beamlines/sis/~>.
- [59] M.R. Presland, J.L. Tallon, R.G. Buckley, R.S. Liu, and N.E. Flower. General trends in oxygen stoichiometry effects on  $T_c$  in Bi and Tl superconductors. *Physica C*, 176:95–105, 1991.
- [60] M.R. Norman. Magnetic collective mode dispersion in high-temperature superconductors. *Phys. Rev. B*, 63:092509, 2001.
- [61] Todor Mishonov, Savina Savona, and Martin Stoev. LCAO model for 3D Fermi surface of high- $T_c$  cuprate  $\text{Tl}_2\text{Ba}_2\text{CuO}_{6+\delta}$ . *cond-mat/0504290*, 2005.
- [62] O.K. Andersen, A.I. Liechtenstein, O. Jepsen, and F. Paulsen. LDA energy bands, low-energy hamiltonians,  $t'$ ,  $t''$ ,  $t_{\perp}(k)$ , and  $J_{\perp}$ . *J. Phys. Chem. Solids*, 56:1573–1591, 1995.
- [63] J. Mesot, M. Randeria, M.R. Norman, A. Kaminski, H.M. Fretwell, J.C. Campuzano, H. Ding, T. Takeuchi, T. Sato, T. Yokoya, T. Takahashi, I. Chong, T. Terashima, M. Takano, T. Mochiku, and K. Kadowaki. Determination of the Fermi surface in high  $T_c$  superconductors by angle-resolved photoemission spectroscopy. *Phys. Rev. B*, 63:224516, 2001.
- [64] M.R. Norman, H. Ding, M. Randeria, J.C. Campuzano, T. Yokoya, T. Takeuchi, T. Takahashi, T. Mochiku, K. Kadowaki, P. Guptasarma, and D.G. Hinks. Destruction of the Fermi surface in underdoped high- $T_c$  superconductors. *Nature*, 392:157–160, 1998.
- [65] H. Matsui, T. Sato, S.-C. Wang, H.-B. Yang, H. Ding, T. Fujii, T. Watanabe, and A. Matsuda. BCS-like Bogoliubov quasiparticles in high- $T_c$  superconductors observed by angle-resolved

photoemission spectroscopy. *Phys. Rev. Lett.*, 90:217002, 2003.

[66] A. Kanigel, M.R. Norman, M. Randeria, U. Chatterjee, S. Souma, A. Kaminski, H.M. Fretwell, S. Rosenkranz, M. Shi, T. Sato, T. Takahashi, Z.Z. Li, H. Raffy, K. Kadowaki, D. Hinks, L. Ozyuzer, and J.C. Campuzano. Evolution of the pseudogap from Fermi arcs to the nodal liquid. *Nat. Phys.*, 2:447–451, 2006.

[67] H. Ding, M.R. Norman, J.C. Campuzano, M. Randeria, A.F. Bellman, T. Yokoya, T. Takahashi, T. Mochiku, and K. Kadowaki. Angle-resolved photoemission spectroscopy study of the superconducting gap anisotropy in  $\text{Bi}_2\text{Sr}_2\text{CaCu}_2\text{O}_{8+\delta}$ . *Phys. Rev. B*, 54:R9678–R9681, 1996.

[68] D.L. Feng, A. Damascelli, K.M. Shen, N. Motoyama, D.H. Lu, H. Eisaki, K. Shimizu, J.-I. Shimoyama, K. Kishio, N. Kaneko, M. Greven, G.D. Gu, X.J. Zhou, C. Kim, F. Ronning, N.P. Armitage, and Z.-X. Shen. Electronic structure of the trilayer cuprate superconductor  $\text{Bi}_2\text{Sr}_2\text{Ca}_2\text{Cu}_3\text{O}_{10+\delta}$ . *Phys. Rev. Lett.*, 88:107001, 2002.

[69] N.J.C. Ingle, K.M. Shen, F. Baumberger, W. Meevasana, D.H. Lu, Z.-X. Shen, A. Damascelli, S. Nakatsuji, Z.Q. Mao, Y. Maeno, T. Kimura, and Y. Tokura. Quantitative analysis of  $\text{Sr}_2\text{RuO}_4$  angle-resolved photoemission spectra: Many-body interactions in a model Fermi liquid. *Phys. Rev. B*, 72:205114, 2005.

[70] A. Damascelli, D.H. Lu, and Z.-X. Shen. From mott insulator to overdoped superconductor: Evolution of the electronic structure of cuprates studied by ARPES. *J. Electron Spectrosc. Relat. Phenom.*, 117–118:165–187, 2001.

[71] A. Kaminski, S. Rosenkranz, H.M. Fretwell, J. Mesot, M. Randeria, J.C. Campuzano, M.R. Norman, Z.Z. Li, H. Raffy, T. Sato, T. Takahashi, and K. Kadowaki. Identifying the background signal in angle-resolved photoemission spectra of high-temperature cuprate superconductors. *Phys. Rev. B*, 69:212509, 2004.

[72] K. Yang, B.P. Xie, D.W. Shen, J.F. Zhao, H.W. Ou, J. Wei, S. Wang, Y.H. Wang, D.H. Lu, R.H. He, M. Arita, S. Qiao, A. Ino, H. Namatame, M. Taniguchi, F.Q. Xu, N. Kaneko, H. Eisaki, and D.L. Feng. Normal state electronic structure in the heavily overdoped regime of  $\text{Bi}_{1.74}\text{Pb}_{0.38}\text{Sr}_{1.88}\text{CuO}_{6+\delta}$  single-layer cuprate superconductors. *Phys. Rev. B*, 73:144507, 2006.

[73] X.J. Zhou, T. Yoshida, D.-H. Lee, W.L. Yang, V. Brouet, F. Zhou, W.X. Ti, J.W. Xiong, Z.X. Zhao, T. Sasagawa, T. Kakeshita, H. Eisaki, S. Uchida, A. Fujimori, Z. Hussain, and Z.-X. Shen. Dichotomy between nodal and antinodal quasiparticles in underdoped  $(\text{La}_{2-x}\text{Sr}_x)\text{CuO}_4$  superconductors. *Phys. Rev. Lett.*, 92:187001, 2004.

[74] S. Sahrakorpi, M. Lindroos, R.S. Markiewicz, and A. Bansil. Evolution of midgap states and residual three dimensionality in  $\text{La}_{2-x}\text{Sr}_x\text{CuO}_4$ . *Phys. Rev. Lett.*, 95:157601, 2005.

[75] A. Kaminski, H.M. Fretwell, M.R. Norman, M. Randeria, S. Rosenkranz, U. Chatterjee, J.C. Campuzano, J. Mesot, T. Sato, T. Takahashi, T. Terashima, M. Takano, K. Kadowaki, Z.Z. Li, and H. Raffy. Momentum anisotropy of the scattering rate in cuprate superconductors. *Phys. Rev. B*, 71:014517, 2005.

[76] A.P. Mackenzie, S.R. Julian, A.J. Diver, G.J. McMullan, M.P. Ray, G.G. Lonzarich, Y. Maeno, S. Nishizaki, and T. Fujita. Quantum oscillations in the layered perovskite superconductor  $\text{Sr}_2\text{RuO}_4$ . *Phys. Rev. Lett.*, 76:3786–3789, 1996.

[77] C. Bergemann, S.R. Julian, A.P. Mackenzie, S. NishiZaki, and Y. Maeno. Detailed topography of the Fermi surface of  $\text{Sr}_2\text{RuO}_4$ . *Phys. Rev. Lett.*, 84:2662–2665, 2000.

[78] A. Damascelli, D.H. Lu, K.M. Shen, N.P. Armitage, R. Ronning, D.L. Feng, C. Kim, Z.-X. Shen, T. Kimura, Y. Tokura, Z.Q. Mao, and Y. Maeno. Fermi surface, surface states and surface reconstruction in  $\text{Sr}_2\text{RuO}_4$ . *Phys. Rev. Lett.*, 85:5194–5197, 2000.

[79] A. Liebsch. Fermi surface, surface states and surface reconstruction in  $\text{Sr}_2\text{RuO}_4$ . *Phys. Rev. Lett.*, 87:239701, 2001.

[80] A. Damascelli, K.M. Shen, D.H. Lu, and Z.-X. Shen. Fermi surface, surface states and surface reconstruction in  $\text{Sr}_2\text{RuO}_4$ . *Phys. Rev. Lett.*, 87:239702, 2001.

[81] K.M. Shen, A. Damascelli, D.H. Lu, N.P. Armitage, R. Ronning, D.L. Feng, C. Kim, Z.-X. Shen, D.J. Singh, I.I Mazin, S. Nakatsuji, Z.Q. Mao, Y. Maeno, T. Kimura, and Y. Tokura. Surface

electronic structure of  $\text{Sr}_2\text{RuO}_4$ . *Phys. Rev. B (Rapid Comm.)*, 64:180502(R), 2001.

- [82] M. Abdel-Jawad, M.P. Kennett, L. Balicas, A. Carrington, A.P. Mackenzie, R.H. McKenzie, and N.E. Hussey. Anisotropic scattering and anomalous transport in a high temperature superconductor. *submitted*, 2006.
- [83] J.A. Slezak and J.C. Davis. *APS March Meeting 2006, invited talk within the focused session 'The electronic properties of overdoped cuprates: the clean gateway to high- $T_c$  superconductivity'*, 2006.
- [84] J.E. Hoffman, K. McElroy, D.-H. Lee, K.M. Lang, H. Eisaki, S. Uchida, and J.C. Davis. Imaging quasiparticle interference in  $\text{Bi}_2\text{Sr}_2\text{CaCu}_2\text{O}_{8+\delta}$ . *Science*, 297:1148–1151, 2002.
- [85] E. Abrahams and C.M. Varma. What angle-resolved photemission experiments tell about the microscopic theory for high-temperature superconductors. *Proc. Natl. Acad. Sci. U. S. A.*, 97:5714–5716, 2000.
- [86] L. Zhu, P.J. Hirschfeld, and D.J. Scalapino. Elastic forward scattering in the cuprate superconducting state. *Phys. Rev. B*, 70:214503, 2004.
- [87] K. Wakabayashi, T.M. Rice, and M. Sigrist. Enhanced coherence of antinodal quasiparticles in a dirty  $d$ -wave superconductor. *Phys. Rev. B*, 72:214517, 2005.
- [88] Matthias Vojta, Ying Zhang, and Subir Sachdev. Quantum phase transitions in  $d$ -wave superconductors. *Phys. Rev. Lett.*, 85:4940–4943, 2000.
- [89] A. Kopp, A. Ghosal, and S. Chakravarty. Competing ferromagnetism in high temperature copper oxide superconductors. *cond-mat/0606431*, 2006.